SERDP

FINAL REPORT

Finite Element Modeling of Scattering from Underwater Buried and Proud Munitions

Ahmad Abawi
Heat, Light, and Sound Research, Inc.

Kyle Becker
ONR

January 2022

SERDP Project MR-2408

REPORT DOCUMENTATION PAGE

Form Approved
OMB No. 0704-0188

1. REPORT DATE *(DD-MM-YYYY)*	**2. REPORT TYPE**	**3. DATES COVERED** *(From - To)*
30/09/2020	SERDP Final Report	3/7/2014 - 3/6/2017

4. TITLE AND SUBTITLE

Finite Element Modeling of Scattering from Underwater Proud and Buried Military Munitions

5a. CONTRACT NUMBER
14-C-0010

5b. GRANT NUMBER

5c. PROGRAM ELEMENT NUMBER

6. AUTHOR(S)
Ahmad Abawi: Heat, Light, and Sound Research, Inc.
Kyle Becker: ONR

5d. PROJECT NUMBER
MR-2408

5e. TASK NUMBER

5f. WORK UNIT NUMBER

7. PERFORMING ORGANIZATION NAME(S) AND ADDRESS(ES)
Heat, Light, and Sound Research, Inc.
12526 High Bluff Dr., Suite 211
San Diego, CA 92130

8. PERFORMING ORGANIZATION REPORT NUMBER
MR-2408

9. SPONSORING/MONITORING AGENCY NAME(S) AND ADDRESS(ES)
Strategic Environmental Research and Development Program (SERDP)
4800 Mark Center Drive, Suite 16F16
Alexandria, VA 22350-3605

10. SPONSOR/MONITOR'S ACRONYM(S)
SERDP

11. SPONSOR/MONITOR'S REPORT NUMBER(S)
MR-2408

12. DISTRIBUTION/AVAILABILITY STATEMENT
DISTRIBUTION STATEMENT A. Approved for public release: distribution unlimited.

13. SUPPLEMENTARY NOTES

14. ABSTRACT
Develop high fidelity acoustic scattering models to facilitate the detection, localization, and characterization of military munitions found in ponds, lakes, rivers, estuaries, and coastal ocean areas. Use these models to design experiments, interpret collected data, identify features that can be used in training classifiers.
The objective of this work has been to develop high fidelity acoustic scattering models that can quickly compute the acoustic color templates (backscattered target strength as a function of frequency and aspect angle) for UXO targets. These models are used to design experiments, interpret collected data and particularly identify features that can be used in classification.

15. SUBJECT TERMS
Finite Element Modeling, Scattering, Underwater Proud, Buried Military Munitions

16. SECURITY CLASSIFICATION OF:			**17. LIMITATION OF ABSTRACT**	**18. NUMBER OF PAGES**	**19a. NAME OF RESPONSIBLE PERSON**
a. REPORT	**b. ABSTRACT**	**c. THIS PAGE**			Ahmad Abawi
UNCLASS	UNCLASS	UNCLASS	UNCLASS	35	**19b. TELEPHONE NUMBER** *(Include area code)* 858-336-6409

SERDP Final Report

Contents

List of Figures

Abstract

Objectives: Develop high fidelity acoustic scattering models to facilitate the detection, localization, and characterization of military munitions found in ponds, lakes, rivers, estuaries, and coastal ocean areas. Use these models to design experiments, interpret collected data, identify features that can be used in training classifiers.

Technical Approach: Most acoustic scattering models are well-equipped to compute scattering from elastic objects in free space. However, unexploded ordnance (UXO) reside in complex ocean environments, which have a profound effect on their acoustic response to sonar. Thus, in trying to model the response of UXO to sonar, a high-fidelity model must account for the interaction between the target and its surrounding environment. While the standard method of solution for an arbitrary elastic target is the finite element method, the solution of the scattering problem in the surrounding medium is best handled by the boundary integral equation, as it replaces the infinite domain problem by an integral over the surface of the target. Furthermore, the boundary integral method has the advantage of reducing the dimensionality of the problem by one. In contrast, the finite element method is not well-suited for solving the scattering problem in the surrounding environment due to difficulty in satisfying the radiation condition. For these reasons, we solve the problem of scattering from an elastic target in a complex ocean environment by a combination of finite element method and boundary integral method. We use the finite element method to model the motion of the target by computing its impedance matrix in vacuum, and the boundary integral method to model the acoustic field in its surrounding medium. The two solutions are coupled by satisfying the required boundary conditions on the surface of the target. This results in a model that treats the interaction between the target and its surrounding environment exactly. We refer to our model as the Coupled Finite Element /Boundary Element method or CFEBE.

Results: This project has been active since 2013. During its first three years, we provided benchmark-quality solutions for various targets to researchers within SERDP who do similar type of modeling. While doing this, an important part of our work was to validate our own models using analytical solutions when available and other well-tested solutions. We validated our 3D and axially-symmetric models in free space using the analytic solution for elastic spheres and spherical shells. We also validated our models for scattering from a proud, half-buried and a fully-buried solid sphere by comparing our results with those of the T-matrix method. We computed the acoustic color (backscattered target strength as function of frequency and angle of incidence) for the aluminum replica of a UXO (henceforth aluminum UXO), the Bullet-105 and the Howitzer shell in free space using both our 3D and axially-symmetric versions of the CFEBE model. We computed the acoustic color for the fully proud and the fully buried aluminum UXO and compared our results with measurements and those produced by other models. Additionally, we computed the acoustic color for the partially buried aluminum UXO and again compared our results with other finite element models since measured results for this case was not yet available. The model results in all cases agreed with each other and and with the measurements.

Since 2017 this project has been co-funded by ONR and SERDP. This report concerns achievements made during this phase of the project, but to make it self-contained, important results are included in the appendix. The report is divided into two parts: In the first part, we list the work that went into improving the CFEBE model and in the second part we describe new model

applications. Our most significant accomplishment during this period is the development of a new approach to compute the acoustic color in two half-spaces. This approach is based on using a multipole solution to represent the spectral Green's functions, which results in significant reduction in computation time. We also laid the groundwork for the implementation of the method of $\mathscr{H}$-Matrices. This method is a hierarchical method of matrix partitioning, which promises to reduce both storage and computation time from $\mathscr{O}(n^2)$ to $\mathscr{O}(n\log n)$, where n is the size of matrices involved. For a typical problem, the reduction in computation time could be as much as a factor of two thousand without noticeable degradation in accuracy. We anticipate that full implementation of this method would be a game changer in modeling scattering from UXOs. We also implemented the Burton-Miller method, which is a method that ensures that the boundary element equations have unique solutions. So far, we have been using the alternative Combined Helmholtz Integral Equation Formulation (CHIEF) method to do this, but this method results in non-square matrices, which cannot be used by $\mathscr{H}$-Matrices. In the second part of the report, we describe new applications of the CFEBE model in computing the acoustic color for UXOs in slightly more complex environments and for arbitrary burial. We also describe the application of the model to compute scattering from multiple targets and scattering from a non-axially symmetric mortar shell.

Benefits: The CFEBE method has several advantages over currently-used methods. The most important ones are: 1) The method is inherently broadband since the stiffness and mass matrices, which constitute the impedance matrix, are independent of frequency. Therefore, the computation of these matrices, which makes up the most numerically intensive part of the computation, is performed once for all frequencies. 2) This method is efficient because it requires a matrix inversion for each frequency, but not each angle while computing the acoustic color. This is not the case for currently-used methods, which must solve a full finite element problem for each frequency and each angle of incidence. 3) Since this method computes the target impedance matrix in vacuum, the same impedance matrix can be used in any environment, so changing the environment for the same target does not require a full finite element solution of the problem. 4) By projecting the impedance matrix onto the surface nodes, this method reduces a finite element problem to a boundary element problem with far fewer unknowns. This reduction in the number of unknowns enables the method to solve a 3D problem with ease. 5) It provides a numerically exact solution since it self-consistently couples the target with the surrounding environment. 6) Due its modular nature, the method easily lends itself to parallel processing.

1 Objective

The objective of this work has been to develop high fidelity acoustic scattering models that can quickly compute the acoustic color templates (backscattered target strength as a function of frequency and aspect angle) for UXO targets. These models are used to design experiments, interpret collected data and particularly identify features that can be used in classification.

2 Background

Modeling the response of UXOs to a sonar signal in an ocean environment belongs to a large class of problems referred to as the fluid-structure interaction, where the fluid in this case refers to the ocean environment and the structure refers to the UXO. The problem of determining the interaction between a submerged elastic structure and its surrounding fluid is of considerable interest, particularly in underwater acoustics and aeronautics where it is required to determine the acoustic field about an arbitrary three-dimensional structure. While the standard method of solution for an arbitrary elastic structure is the finite element method, the solution of the reduced wave equation in the surrounding medium is best handled by the boundary integral equation, as it replaces the infinite domain problem by an integral over the surface of the submerged structure. Furthermore, the boundary integral method has the advantage of reducing the dimensionality of the problem by one. In contrast, the finite element method is not well-suited for solving the wave equation in the surrounding fluid environment due to difficulty in satisfying the radiation condition as well as demands on the mesh size and the difficulty in generating the fluid mesh.

For these reasons the problem of fluid-structure interaction is perhaps best treated by a combination of finite element method to model the motion of the structure and the boundary integral method to model the acoustic field in its surrounding medium, where the coupling between the two models is achieved by imposing the continuity of pressure and normal particle velocity at the surface of the structure.

The coupled finite and boundary integral method has been used by several authors in recent years [1]-[2] and (see Amini *et al.* [3] and the references therein). The main differences in these approaches are the particular finite element package and boundary integral formulation employed, the numerical approximation used and the details of the method of coupling.

In this work [2], we use the CFEBE model to compute the scattered acoustic field from an arbitrary elastic structure in an arbitrary medium, characterized by a Green's function. The formulation (also known as the impedance formulation) results in a self-consistent, accurate, and numerically efficient solution that is valid in any environment. In modeling the structure, we use hexahedral eight-node elements to discretize the Galerkin weighted residual equation and in modeling the acoustic environment, we discretize the Helmholtz-Kirchhoff equation by expanding pressure and normal particle velocity in piecewise constant basis functions over quadrilateral elements on the surface of the structure. The finite and boundary element solutions are coupled by imposing the continuity of pressure and normal particle velocity on the surface nodes of the structure.

During the first phase of the project (2013-2017), the CFEBE model was developed, implemented and validated. The CFEBE model is a 3D model, which means that it can be applied to targets of arbitrary shape in arbitrary ocean environments. We also developed an axially-symmetric version of it to compute scattering from axially-symmetric structures with non-axially-symmetric loading that is significantly faster. We validated both models using analytic solutions for spheres in free space and the T-matrix solution in two half spaces. A Final Report for this phase of the project was submitted to SERDP in 2017.

Model improvements and its new applications achieved during the current phase of the project (2017-2020) are described below.

3 Model Improvements

3.1 Computation of scattering in two half-spaces

A complex environment is defined as one that is not free space. In most SERDP applications, the ocean environment can be well-approximated by two isovelocity half spaces: a water half-space with sound speed c_1 and density ρ_1 over a bottom half-space with sound speed c_2, density ρ_2, and interface at $z = 0$. The Green's function for this environment is given by

$$G(r,z;r_s,z_s) = \int_0^\infty \tilde{G}(k_r,z;z_s) J_0(k_r|r-r_s|) k_r dk_r, \tag{1}$$

where r_s and z_s are the source range and depth and r and z are the receiver range and depth, J_0 is the Bessel function of order zero and the spectral Green's function $\tilde{G}(k_r,z;z_s)$ for a source located in the water is given by

$$\tilde{G}(k_r,z;z_s) = \begin{cases} \dfrac{i\mathbb{R}e^{ik_{z_1}(z+z_s)}}{4\pi k_{z_1}} + \tilde{g}_w(k_1,r,k_z;r_s,z_s) & \text{for} \quad z \geq 0, \\ \dfrac{i\mathbb{T}_{12}e^{ik_{z_1}z_s}e^{-ik_{z_2}z}}{4\pi k_{z_1}} & \text{for} \quad z < 0, \end{cases} \tag{2}$$

where $k_{z_1} = \sqrt{k_1^2 - k_r^2}$, $k_{z_2} = \sqrt{k_2^2 - k_r^2}$, ω is the circular frequency and the reflection and transmission coefficients are given by

$$\mathbb{R} = \frac{k_{z_1}\rho_2 - k_{z_2}\rho_1}{k_{z_1}\rho_2 + k_{z_2}\rho_1}, \quad \mathbb{T}_{12} = \frac{2k_{z_1}\rho_2}{k_{z_1}\rho_2 + k_{z_2}\rho_1}, \quad k_i = \frac{\omega}{c_i},\ i = 1,2,$$

and

$$\tilde{g}_w(k,r,k_z;r_s,z_s) = \frac{i}{4\pi}\frac{e^{ik_z|z-z_r|}}{k_z},$$

is the spectral free space Green's function. It is related to the free space Green's function via the Sommerfeld-Wyle integral

$$g_w(k,r,z;r_s,z_s) = \int_0^\infty \tilde{g}_w(k,r,k_z;r_s,z_s) J_0(k_r|r-r_s) k_r dk_r = \frac{e^{ik\sqrt{(r-r_s)^2+(z-z_s)^2}}}{4\pi\sqrt{(r-r_s)^2+(z-z_s)^2}}. \tag{3}$$

The above Green's functions are used in Eqs. (A-2) and (A-15) to compute the scattered field at the receiver.

The matrices **A** and **B** in Eq. (A-2) account for the interaction between surface elements, where one element plays the role of the source and the other the role of the receiver in the expressions for the spectral Green's functions. Similarly, in computing the scattered field, the surface elements play the role of the sources. For this reason, if the entire target or any part of it is in the bottom half space, we need a spectral Green's function for a source in the bottom, which is given by

$$\tilde{G}(k_r,z;z_s)=\begin{cases}\dfrac{i\mathbb{T}_{21}e^{ik_{z_1}z}e^{-ik_{z_2}z_s}}{4\pi k_{z_2}} & \text{for} \quad z\geq 0,\\[2ex] \dfrac{-i\mathbb{R}e^{-ik_{z_2}(z+z_s)}}{4\pi k_{z_2}}+\tilde{g}_w(k_2,r,k_z;r_s,z_s) & \text{for} \quad z<0,\end{cases} \tag{4}$$

where now the reflection and transmission coefficients are given by

$$\mathbb{R}=-\frac{k_{z_1}\rho_2-k_{z_2}\rho_1}{k_{z_1}\rho_2+k_{z_2}\rho_1}, \qquad \mathbb{T}_{21}=\frac{2k_{z_2}\rho_1}{k_{z_1}\rho_2+k_{z_2}\rho_1}.$$

By substituting Eq. (2) and Eq. (4) in Eq. (1), we obtain for the source in the water

$$G(r,z;r_s,z_s)=\begin{cases}\displaystyle\int_0^\infty \frac{i\mathbb{R}e^{ik_{z_1}(z+z_s)}}{4\pi k_{z_1}}J_0(k_r|r-r_s|)k_r dk_r+g_w(k_1,r,z;r_s,z_s) & \text{for} \quad z\geq 0,\\[2ex] \displaystyle\int_0^\infty \frac{i\mathbb{T}_{12}e^{ik_{z_1}z_s}e^{-ik_{z_2}z}}{4\pi k_{z_1}}J_0(k_r|r-r_s|)k_r dk_r & \text{for} \quad z<0,\end{cases} \tag{5}$$

and for the source in the bottom

$$G(r,z;r_s,z_s)=\begin{cases}\displaystyle\int_0^\infty \frac{i\mathbb{T}_{21}e^{ik_{z_1}z}e^{-ik_{z_2}z_s}}{4\pi k_{z_2}}J_0(k_r|r-r_s|)k_r dk_r & \text{for} \quad z\geq 0,\\[2ex] \displaystyle\int_0^\infty \frac{-i\mathbb{R}e^{-ik_{z_2}(z+z_s)}}{4\pi k_{z_2}}J_0(k_r|r-r_s|)k_r dk_r+g_w(k_2,r,z;r_s,z_s) & \text{for} \quad z<0.\end{cases} \tag{6}$$

The computation of matrices **A** and **B** requires n^2 evaluations of the Green's functions, where n is the number of surface elements. For a typical target, we have anywhere between 6 to 20 thousand surface elements, which means that the computation of these matrices requires on the order of one hundred million function evaluations. This becomes a daunting numerical task when the Green's functions are represented in terms of spectral integrals as in Eqs. (5) and (6). For a target located entirely in the water, the Green's function is given by the top equation in Eq. (5) and for one located entirely in the bottom it is given by the bottom equation in Eq. (6). We note that in these two cases the Green's functions are a function of the sum of source and receiver depths, $(z+z_s)$, and the difference of their ranges, $|r-r_s|$. So in these two cases, the Green's functions are a function of two parameters, which allows for the use of 2D interpolation. For the cases of fully proud and fully buried targets, we computed the Green's functions on a 200×200 grid as a function of the sum of source and receiver depths and the difference of their ranges around the target, and computed their values at the surface elements using two-parameter interpolation. This essentially reduced

the number of function evaluations from 10^8 to 10^4 and proved to be a crucial step in our ability to compute the acoustic color for targets of interest.

For the case of a partially buried target, the situation is more complicated. Referring to the bottom equation in Eq. (5) and the top equation in Eq. (6), we see that in this case the Green's functions are a function of source depth, z_s, receiver depth, z, and the difference between their ranges, $|r - r_s|$. This would require a 3-parameter interpolation, which is an extremely expensive numerical process. One way to deal with this numerical complexity is to divide the interaction matrix into four submatrices: one containing those source elements and receiver elements that reside in the water, the other containing those that reside in the bottom and two other submatrices where the source elements are in the water and the receiver elements are in the bottom and vice versa. Again, since both the source and the receiver elements are in the same medium, interpolation can be used for the first two submatrices, but for the other two a direct computation would be necessary, albeit on smaller matrices. But even that is a very expensive numerical process.

One of our most significant accomplishment during this project is to recast equations Eqs. (2-6) in terms of multipole expansions, which significantly reduces numerical computation. For source and receiver in the water, the Green's function can be written as

$$G(r,z,\varphi;r_s,z_s,\varphi_s) = \sum_{n=0}^{\infty} \varepsilon_n \int_0^{\infty} \frac{i\mathbb{R} e^{ik_{z_1} z_s} e^{ik_{z_1} z}}{4\pi k_{z_1}} J_n(k_r r_s) J_n(k_r r) \cos\left[n(\varphi_s - \varphi)\right] k_r dk_r + g_w(k_1, r, z; r_s, z_s),\ (z,\ z_s > 0), \tag{7}$$

and for source and receiver in the bottom it can be written as

$$G(r,z,\varphi;r_s,z_s,\varphi_s) = \sum_{n=0}^{\infty} \varepsilon_n \int_0^{\infty} \frac{-i\mathbb{R} e^{ik_{z_2} z_s} e^{ik_{z_2} z}}{4\pi k_{z_1}} J_n(k_r r_s) J_n(k_r r) \cos\left[n(\varphi_s - \varphi)\right] k_r dk_r + g_w(k_2, r, z; r_s, z_s),\ (z,\ z_s < 0). \tag{8}$$

The Green's functions for the transmitted field from water to bottom is given by

$$G(r,z,\varphi;r_s,z_s,\varphi_s) = \sum_{n=0}^{\infty} \varepsilon_n \int_0^{\infty} \frac{i\mathbb{T}_{12} e^{ik_{z_1} z_s} e^{-ik_{z_2} z}}{4\pi k_{z_1}} J_n(k_r r_s) J_n(k_r r) \times \cos\left[n(\varphi_s - \varphi)\right] k_r dk_r,\ z_s \geq\ z < 0, \tag{9}$$

and from bottom to water is given by

$$G(r,z,\varphi;r_s,z_s,\varphi_s) = \sum_{n=0}^{\infty} \varepsilon_n \int_0^{\infty} \frac{i\mathbb{T}_{21} e^{ik_{z_1} z} e^{-ik_{z_2} z_s}}{4\pi k_{z_2}} J_n(k_r r_s) J_n(k_r r) \times \cos\left[n(\varphi_s - \varphi)\right] k_r dk_r,\ z_s < 0\ z \geq 0. \tag{10}$$

Note that the cosine terms in the above equations can be written as $\cos n\varphi_s \cos n\varphi + \sin n\varphi_s \sin n\varphi$. Equations (7-10) have a remarkable property that each term is either a function of the source location or receiver location and there is no term that contains both. This allows these equations to be written in terms of outer products, which require only $2Mn$ functions evaluations compared

to n^2 function evaluations had Eq. (5) and Eq. (6) been used. M is the maximum number of terms in the sums in Eqs. (7-10) and it is on the order 50. Thus for $n \sim 10000$, the previous formulation requires 10^8 while the new formulation only requires 10^6 function evaluations. Actual improvements in execution times for computing the acoustic color for a proud, partially buried and fully buried aluminum replica of a UXO are shown in Fig. (1). Note that substantial speed improvement can be seen across the board, but while this improvement is about 3.5 times for the cases of a fully proud and a fully buried UXO (the left and right panels), it is about 8.5 times for the case of a partially buried UXO (middle panel). The reason for this is that the former two cases still benefit from interpolation and do not have much room for speed improvement, but, as was discussed in the above, this is not the case for a partially buried target where there is little benefit from interpolation.

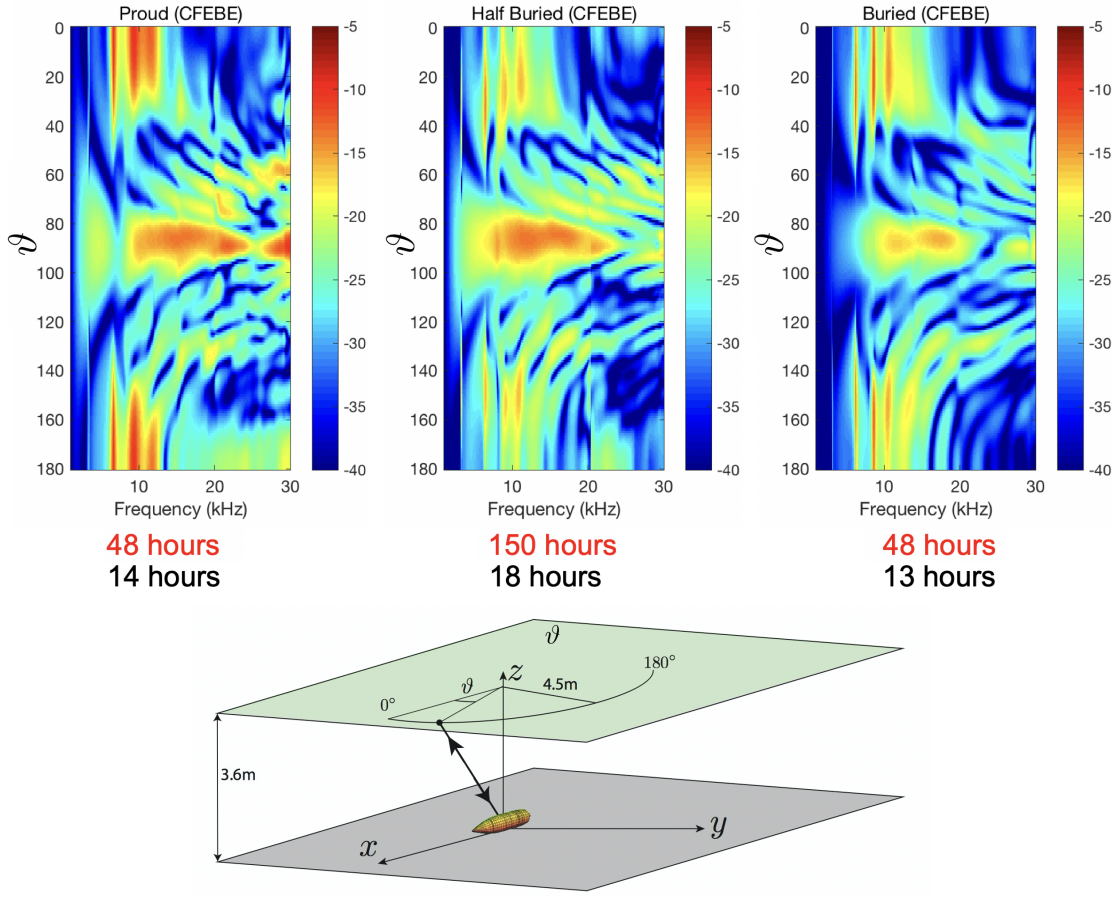

Figure 1: *Comparison of execution times for computing the acoustic color template for the aluminum replica of a UXO. The execution times in red are for the case when the spectral Green's function were represented by Eqs. (5-6) and those in black are for the case when the multipole representations in Eqs. (7-10) are used. The scattering geometry is shown in the bottom figure.*

3.2 Towards the implementation of $\mathscr{H}$-Matrices

Solution of the boundary element problem requires solving the system of linear equation $\mathbf{Mx} = \mathbf{b}$, where the matrix $\mathbf{M}$ can be a combination of matrices $\mathbf{A}$ and $\mathbf{B}$, which are large, complex and

dense. These matrices require $\mathcal{O}(n^2)$ units of storage and that many function evaluations (assembly), where n is the number of surface elements. The assembly and computation of these matrices require an enormous amount computer processing and storage. It is assumed within the framework of the method of $\mathscr{H}$-Matrices [4]-[5], that all sub-blocks of a large dense matrix do not have the same physical significance. For example, sub-blocks near the diagonal of a matrix are more important than those in its outer boundaries since they represent interaction between near elements. $\mathscr{H}$-Matrices is a method of using data-sparse matrices to approximate non-sparse matrices, where a geometrical process is used to systematically partition a matrix into sub-blocks and perform a so-called *admissibility* test using an adjustable parameter η. This test determines whether a sub-block can be represented by low-rank matrices. If the answer is yes, it is deemed as *admissible* and the partitioning stops, otherwise the partitioning continues. The parameter η determines the minimum size of the sub-blocks where the partitioning stops regardless of whether the sub-block is low-rank (*admissible*) or full rank. Larger values of η results in smaller sub-blocks. After the partitioning is completed, the resulting matrix is referred to as an $\mathscr{H}$-matrix. This method reduces both storage and assembly to $\mathcal{O}(n\log n)$, i.e. for a typical $n \sim 10000$, both storage and assembly reduce from $\sim 10^8$ to $\sim 10^4$, an amazing factor of 10000! $\mathscr{H}$-matrices are special type of matrices with their own customized linear algebra for matrix operations that provide approximate variants of the usual matrix operations such as addition, multiplication, and inversion with almost linear complexity. Thus, in order to take full advantage of its power, one would need to use these customized routines for matrix operations. These routines are available in a publicly-accessible library called H2Lib (`http://www.h2lib.org/`).

Figure (2) shows the schematics of how an $\mathscr{H}$-matrix is obtained by repeated partitioning.

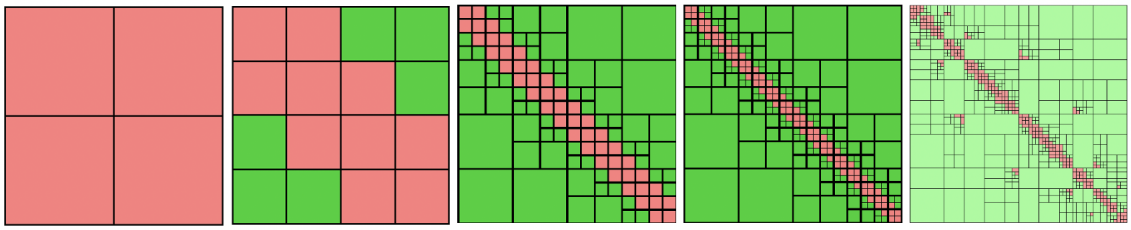

Figure 2: *Partitioning of a matrix using the method of $\mathscr{H}$-matrices. Red blocks are filled with the exact and green blocks are filled with the much cheaper, low-rank representation of the kernel, resulting in much faster matrix assembly time and much smaller storage.*

There is a direct relationship between the way a matrix is partitioned by the method of $\mathscr{H}$-matrices and the rank of its sub-blocks. The left two panels in Fig. (3) are partitioned using the routines in H2Lib. They represent the $\mathscr{H}$-matrices for the interaction matrix, Eq. (A-13), for an aluminum replica of a UXO in free space, partitioned using two values of the parameter η. The right panel shows the ranks of its sub-blocks. The matrix in the right panel is 5900×5900 and the sub-blocks contain 59×59 elements, so the full matrix is divided into 100×100 sub-blocks and the rank of each sub-block is computed. In the left two panels, the white color represents admissible (low rank) and the red color represents full rank sub-blocks. In the right panel higher rank sub-blocks are also represented by the red color. The resemblance between these figures confirms that the hierarchy of the sub-blocks is based on their rank.

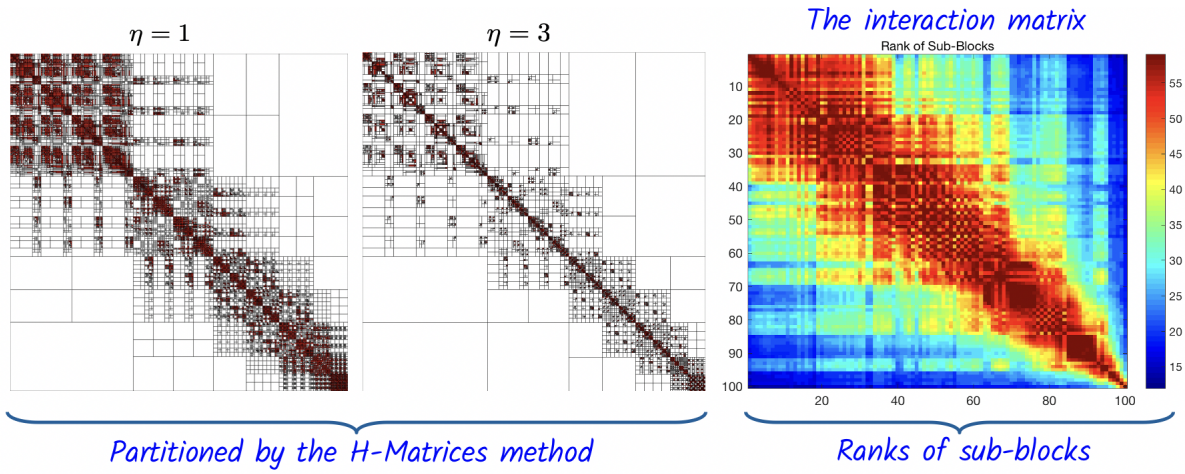

Figure 3: *The left two panels are partitioned using the routines in H2Lib. They are the $\mathscr{H}$-matrices representation of the interaction matrix for two values of the parameter η, which controls the minimum size of sub-blocks. η determines the minimum size of the sub-blocks beyond which the partitioning stops. In the right panel, the rank of the interaction matrix is computed for an array of 100×100 sub-blocks, each containing 59×59 elements.*

We applied $\mathscr{H}$-matrices to the solution of Laplace equation (not shown) and demonstrated that almost linear complexity of $\mathscr{O}(n \log n)$ can be achieved. As an application of the method to the Helmholtz equation, Fig. (4) shows the timing graph as a function of the size of the matrix (number of elements, n) for the solution of Eq. (A-12) for a 2:1-foot aluminum cylinder on the left and for a rigid cylinder of the same size on the right using $\mathscr{H}$-matrices. The red and black curves in each figure show the $\mathscr{O}(n^2)$ and the $\mathscr{O}(n \log n)$ growth rate, respectively. We expect solutions involving full matrices to have a growth rate close to $\mathscr{O}(n^2)$ and those involving $\mathscr{H}$-matrices to have a growth rate close to $\mathscr{O}(n \log n)$. It can be seen that this is achieved for the case of a rigid cylinder, but for the solution of the aluminum cylinder the growth rate is still close to $\mathscr{O}(n^2)$.

To understand the reason behind this, note that Eq. (A-12) for an elastic object can be written as

$$\mathbf{p} = (\mathbf{A} - i\omega \mathbf{B}\boldsymbol{\Gamma})^{-1} \mathbf{p}_{inc}, \tag{11}$$

where

$$\boldsymbol{\Gamma} \equiv \mathbf{L} \left(-\omega^2 \mathbf{M} + \mathbf{K}\right)^{-1} \mathbf{L}^{\mathrm{T}}. \tag{12}$$

For a rigid object Eq. (11) reduces to

$$\mathbf{p} = \mathbf{A}^{-1} \mathbf{p}_{inc}. \tag{13}$$

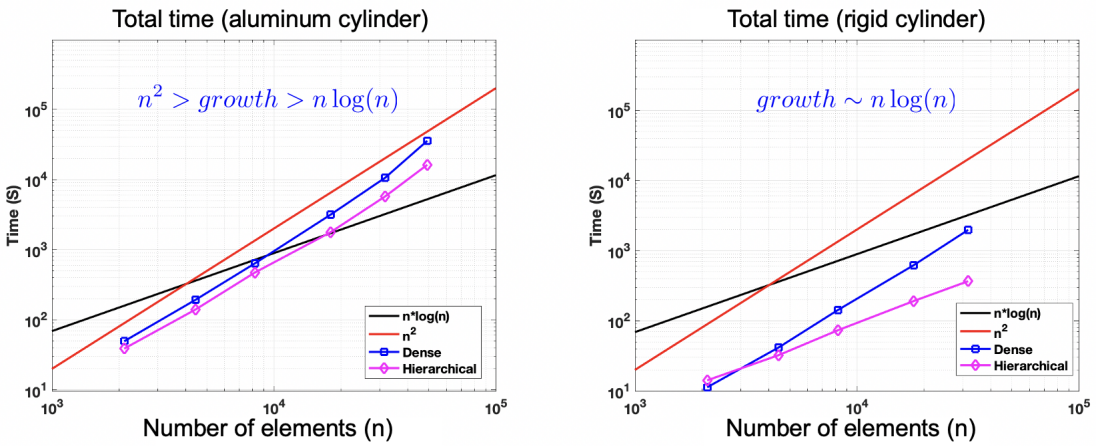

Figure 4: *The growth rate for the solution of (A-12) using $\mathscr{H}$-matrices for the for a 2:1-foot aluminum cylinder on the left and for a rigid cylinder on the right. Note that a linear growth rate of $\mathscr{O}(n\log n)$ is achieved for the rigid cylinder, but for the case of the aluminum cylinder it is still close to $\mathscr{O}(n^2)$.*

Since both matrices $\mathbf{A}$ and $\mathbf{B}$ can be converted to $\mathscr{H}$-matrices, the solution of Eq. (13) for a rigid object takes full advantage of the method and its growth rate is close to $\mathscr{O}(n\log n)$, as can be seen in the right panel of Fig. (4). The solution for an elastic object is obtained from Eq. (11). In this case, the matrix $\mathbf{\Gamma}$ is a dense matrix, which does not lend itself to be converted to an $\mathscr{H}$-matrix, and since the product of an $\mathscr{H}$-matrix, $\mathbf{B}$, and a dense matrix, $\mathbf{\Gamma}$, is still a dense matrix, Eq. (11) cannot take full advantage of the benefits that the method offers and its growth rate remains close to $\mathscr{O}(n^2)$. Fortunately, this problem can be solved using a different formulation of the boundary element equations, where instead of Eq. (11), the following equation is used

$$\mathbf{p} = \left(\mathbf{A}^{-1}\mathbf{p}_{inc} - i\omega\mathbf{A}^{-1}\mathbf{B}\mathbf{\Sigma}\right), \tag{14}$$

where the derivation of Eq. (14) is given in Appendix A.

Figure (5) shows how the application of H2Lib to the new formulation, Eq. (14), results in a solution that takes full advantage of the method of $\mathscr{H}$-matrices and thus is numerically much more efficient. In the figure, red squares represent full and green squares represent $\mathscr{H}$-matrices. Note that the inability to convert the matrix $\mathbf{\Gamma}$ to an $\mathscr{H}$-matrix in the left column of Fig. (5) results in a solution that still contains a full matrix in the bottom of the left column. In the new formulation, $\mathbf{\Sigma}$ is a column vector and H2Lib is able to convert matrices $\mathbf{A}^{-1}$ and $\mathbf{A}^{-1}\mathbf{B}$ to $\mathscr{H}$-matrices. The result in the bottom of the right column involves an $\mathscr{H}$-matrix, a full column vector and no need to take an inverse!. This solution is much more efficient than the one obtained using the current formulation. However, we have not been able to implement this method yet because H2Lib does not yet have a provision to deal with the non-uniqueness issue that is inherent in all boundary element formulations. This is a well-known problem and there are at least two methods that can fix it. One of these methods is CHIEF [6] and the other is the Burton-Miller method [7]. Our boundary element formulations currently use the CHIEF method, but that results in non-square matrices, which cannot be used in H2Lib. The Burton-Miller method is more complicated, but it does result

in square matrices. We have recently implemented the Burton-Miller method for the purpose of using it with H2Lib. This implementation is discussed in the next section. We plan to provide our implementation to the group that is responsible for maintaining H2Lib and hope that they make it part of the package. At that point we will be able integrate H2Lib with our scattering computation tools.

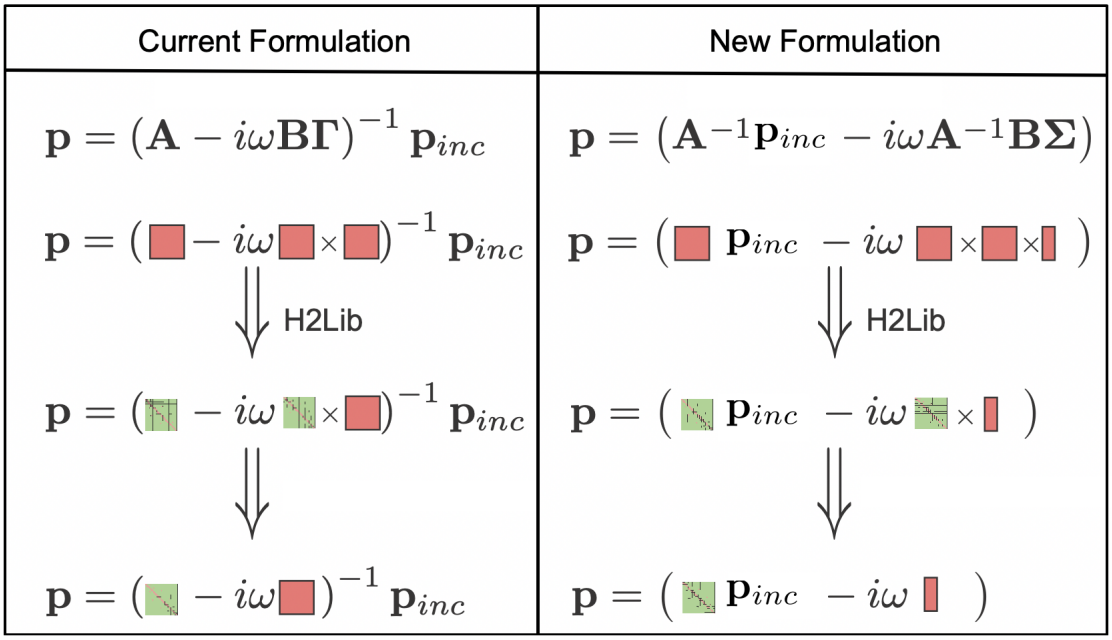

Figure 5: *The applications of H2Lib to the current, Eq. (A-12), and the new, Eq. (14), formulations. Green squares represent $\mathscr{H}$-matrices, red squares represent full matrices and red rectangles represent column vectors. The bottom equation in each column is the final solution for each formulation.*

3.3 The implementation of the Burton-Miller method

The Helmholtz integral equation is given by

$$p_{inc}(\mathbf{x}) + \int_{S'} \left\{ p(\mathbf{x}') \frac{\partial G_k(\mathbf{x},\mathbf{x}')}{\partial \mathbf{n}'} - G_k(\mathbf{x},\mathbf{x}') \frac{\partial p(\mathbf{x}')}{\partial \mathbf{n}'} \right\} dS' = \begin{cases} p(\mathbf{x}), & \mathbf{x} \in \text{E}, \quad (15a) \\ \frac{1}{2} p(\mathbf{x}), & \mathbf{x} \in \text{B}, \quad (15b) \\ 0, & \mathbf{x} \in \text{D}. \quad (15c) \end{cases}$$

where G_k is the free space Green's function for the Helmholtz equation, E denotes the exterior, B the boundary surface and D the interior. A discretized version of the integral term in the above equation is given by Eq. (A-17) in which $\partial p(\mathbf{x}')/\partial \mathbf{n}' = -i\omega\rho v(\mathbf{x}')$ has been used, where v is the normal surface velocity. Defining the integral operators

$$\begin{aligned} L_k[\sigma] &= \int_{S'} \sigma(\mathbf{x}') G_k(\mathbf{x},\mathbf{x}') dS', \qquad \text{(single layer)} \\ M_k[\sigma] &= \int_{S'} \sigma(\mathbf{x}') \frac{\partial G_k(\mathbf{x},\mathbf{x}')}{\partial \mathbf{n}'} dS', \quad \text{(double layer).} \end{aligned} \tag{16}$$

Equation (15b) can then be written

$$\frac{1}{2}p + L_k\left[\frac{\partial p}{\partial n}\right] - M_k[p] = p_{inc},\ (\mathbf{x} \in B). \tag{17}$$

For the Neumann boundary condition ($\partial p/\partial n|_B = 0$), Eq. (17) reduces to

$$\frac{1}{2}p - M_k[p] = 0,\ (\mathbf{x} \in B). \tag{18}$$

For Dirichlet boundary condition, a unique solution of Eq. (15) requires that $p \equiv 0$, which is a trivial solution of Eq. (18). Non-unique solutions occur when Eq. (18) has a non-trivial solution and in what follows (non-unique) and (non-trivial) are used interchangeably. Since p is identically zero in the interior and on the boundary, it implies that $\partial p/\partial n|_B = 0$. But if k coincides with one of eigenvalues of Eq. (18) there exists a non-trivial solution for which $\partial p/\partial n|_B \neq 0$. The latter statement can be verified as follows: first, write the normal derivative of Eq. (15b)

$$\frac{1}{2}\frac{\partial p}{\partial n} - \frac{\partial}{\partial n}L_k\left[\frac{\partial p}{\partial n}\right] + \frac{\partial}{\partial n}M_k[p] = \frac{\partial}{\partial n}p_{inc},\ (\mathbf{x} \in B), \tag{19}$$

Next, evaluate it in the interior

$$\frac{1}{2}\frac{\partial p}{\partial n} - \frac{\partial}{\partial n}L_k\left[\frac{\partial p}{\partial n}\right] + \frac{\partial}{\partial n}M_k[p] = 0,\ (\mathbf{x} \in D), \tag{20}$$

At the boundary where $p = 0$, the above equation is

$$\frac{1}{2}\frac{\partial p}{\partial n} - \frac{\partial}{\partial n}L_k\left[\frac{\partial p}{\partial n}\right] = 0,\ (\mathbf{x} \in B). \tag{21}$$

Equation (21) is referred to as the transpose of Eq. (18) and according to a well-known theorem in the theory of Fredholm integral equations, in the event when Eq. (18) has non-unique solutions, Eq. (21) will also have non-unique solutions and vice versa. According to this theorem when p has non-trivial solutions at certain values of k corresponding to the eigenvalues of the interior Dirichlet problem, its normal derivative, which satisfies Eq. (21) will also have non-trivial solutions.

If we make the same argument about Eq. (21) as we did about Eq. (18), a non-trivial solution of the former corresponds to the eigenvalues of the interior Neumann problem, which again results in a non-unique solution. In short, the solution of the exterior Helmholtz integral equation given by Eq. (15) requires –according to Eq. (15c)– for p to be identically zero in the interior and for $\partial p/\partial n$ to be identically zero on the boundary. But the boundary values of $\partial p/\partial n$ satisfy a complementary equation (Eq. (21)), which can have discrete solutions (eigensolutions) for which $\partial p/\partial n|_B \not\equiv 0$, resulting in non-unique solutions.

From the above arguments it is obvious that neither of the above formulations used by itself can guarantee a unique solution. One way that this problem can be treated is to enforce the surface boundary condition at all frequencies by simultaneously solving the exterior and the interior Helmholtz integral equations (Eqs. (15b) and (15c)). This method is known as the CHIEF

method [6]. The method is implemented by overdetermining the $N \times N$ exterior Helmholtz integral equation (Eq. (15b)) with additional compatible equations based on the interior Helmholtz integral equation (Eq. (15c)) for strategic interior points. The solution of this overdetermined system of equations results in a unique solution. However, it is important to note that the number of interior point must increase as a function of frequency to maintain the accuracy of the solution.

The Burton-Miller method [7] is a more general way of treating the non-uniqueness problem in which a single boundary integral equation is constructed by a superposition of Eq. (17) and Eq. (19) coupled by an adjustable parameter, α,

$$\left(\frac{1}{2} - M_k - \alpha N_k\right)[p] = -\left(\frac{\alpha}{2} + L_k + \alpha M_k^T\right)\left[\frac{\partial p}{\partial n}\right] + p_{inc} + \alpha \frac{\partial p_{inc}}{\partial n}, \tag{22}$$

where

$$\begin{aligned} N_k[\sigma] &= \int_{S'} \sigma(\mathbf{x}') \frac{\partial^2 G_k(\mathbf{x}, \mathbf{x}')}{\partial \mathbf{n} \partial \mathbf{n}'} dS', \\ M_k^T[\sigma] &= \int_{S'} \sigma(\mathbf{x}') \frac{\partial G_k(\mathbf{x}, \mathbf{x}')}{\partial \mathbf{n}} dS'. \end{aligned} \tag{23}$$

Burton and Miller proved that Eq. (22) is guaranteed to have a unique solution as long as α has a non-zero imaginary part. The recommended value for α is $\pm i/k$, where the plus sign is used for $e^{-i\omega t}$ time convention and the minus sign is used for the $e^{i\omega t}$ time convention.

3.3.1 Implementation

All the integrals in Eq. (22), except N_k contain weakly singular kernels whose singularity is at worst $\mathscr{O}(r^{-2})$, where $r = |\mathbf{x} - \mathbf{x}'|$ and $\mathscr{O}$ is the order symbol. The kernel in N_k is hypersingular with a singularity of $\mathscr{O}(r^{-3})$. While weakly singular integrals can be handled using a simple piecewise-constant collocation method, hypersingular integrals require special treatment. In what follows, we describe a regularization method based on the work of Chen and Harris [8], but specialized to flat elements, followed by the use of a special kind of quadrature technique to treat the hypersinular kernel that appears in Eq. (22). By substituting the integral operators defined in Eq. (16) and Eq. (23) in Eq. (22), we obtain

$$\begin{aligned} &\frac{1}{2} p(\mathbf{x}) - \int_{S'} p(\mathbf{x}') \left(\frac{\partial G_k(\mathbf{x}, \mathbf{x}')}{\partial \mathbf{n}'} + \alpha \frac{\partial^2 G_k(\mathbf{x}, \mathbf{x}')}{\partial \mathbf{n} \partial \mathbf{n}'} \right) dS' \\ &= -\frac{\alpha}{2} \frac{\partial p(\mathbf{x})}{\partial \mathbf{n}} - \int_{S'} \frac{\partial p(\mathbf{x}')}{\partial \mathbf{n}'} \left(G_k(\mathbf{x}, \mathbf{x}') + \alpha \frac{\partial G_k(\mathbf{x}, \mathbf{x}')}{\partial \mathbf{n}} \right) dS' + f_{inc}, \end{aligned} \tag{24}$$

where $f_{inc} = p_{inc} + \alpha \partial p_{inc} / \partial n$. Using the identity [9]

$$\int_{S'} \frac{\partial^2 G_k(\mathbf{x}, \mathbf{x}')}{\partial \mathbf{n} \partial \mathbf{n}'} dS' = k^2 \int_{S'} \mathbf{n} \cdot \mathbf{n}' G_k(\mathbf{x}, \mathbf{x}') dS', \tag{25}$$

one can write

$$\int_{S'} p(\mathbf{x}') \frac{\partial^2 G_k(\mathbf{x},\mathbf{x}')}{\partial \mathbf{n} \partial \mathbf{n}'} dS' = \int_{S'} \left(p(\mathbf{x}') - p(\mathbf{x}) \right) \frac{\partial^2 G_k(\mathbf{x},\mathbf{x}')}{\partial \mathbf{n} \partial \mathbf{n}'} dS' + k^2 \int_{S'} p(\mathbf{x}) \mathbf{n} \cdot \mathbf{n}' G_k(\mathbf{x},\mathbf{x}') dS'. \tag{26}$$

Let us write

$$\int_{S'} p(\mathbf{x}') \frac{\partial^2 G_k(\mathbf{x},\mathbf{x}')}{\partial \mathbf{n} \partial \mathbf{n}'} dS' = \int_{S'} p(\mathbf{x}') \left[\frac{\partial^2 G_k(\mathbf{x},\mathbf{x}')}{\partial \mathbf{n} \partial \mathbf{n}'} - \frac{\partial^2 G_0(\mathbf{x},\mathbf{x}')}{\partial \mathbf{n} \partial \mathbf{n}'} \right] dS' + \int_{S'} p(\mathbf{x}') \frac{\partial^2 G_0(\mathbf{x},\mathbf{x}')}{\partial \mathbf{n} \partial \mathbf{n}'} dS', \tag{27}$$

where G_0 is the Green's function for the Laplace equation for which $k = 0$. Equation (26) for $k = 0$ is

$$\int_{S'} p(\mathbf{x}') \frac{\partial^2 G_0(\mathbf{x},\mathbf{x}')}{\partial \mathbf{n} \partial \mathbf{n}'} dS' = \int_{S'} \left(p(\mathbf{x}') - p(\mathbf{x}) \right) \frac{\partial^2 G_0(\mathbf{x},\mathbf{x}')}{\partial \mathbf{n} \partial \mathbf{n}'} dS'. \tag{28}$$

Substituting this into Eq. (27) gives

$$\int_{S'} p(\mathbf{x}') \frac{\partial^2 G_k(\mathbf{x},\mathbf{x}')}{\partial \mathbf{n} \partial \mathbf{n}'} dS' = \int_{S'} p(\mathbf{x}') \left[\frac{\partial^2 G_k(\mathbf{x},\mathbf{x}')}{\partial \mathbf{n} \partial \mathbf{n}'} - \frac{\partial^2 G_0(\mathbf{x},\mathbf{x}')}{\partial \mathbf{n} \partial \mathbf{n}'} \right] dS' + \int_{S'} \left[p(\mathbf{x}') - p(\mathbf{x}) \right] \frac{\partial^2 G_0(\mathbf{x},\mathbf{x}')}{\partial \mathbf{n} \partial \mathbf{n}'} dS'. \tag{29}$$

Finally, by substituting Eq. (29) into Eq. (24) we obtain

$$\frac{1}{2} p(\mathbf{x}) - \int_{S'} p(\mathbf{x}') \frac{\partial G_k(\mathbf{x},\mathbf{x}')}{\partial \mathbf{n}'} dS' - \alpha \left\{ \int_{S'} p(\mathbf{x}') \left[\frac{\partial^2 G_k(\mathbf{x},\mathbf{x}')}{\partial \mathbf{n} \partial \mathbf{n}'} - \frac{\partial^2 G_0(\mathbf{x},\mathbf{x}')}{\partial \mathbf{n} \partial \mathbf{n}'} \right] dS' + \int_{S'} \left[p(\mathbf{x}') - p(\mathbf{x}) \right] \frac{\partial^2 G_0(\mathbf{x},\mathbf{x}')}{\partial \mathbf{n} \partial \mathbf{n}'} dS' \right\} = -\frac{\alpha}{2} \frac{\partial p(\mathbf{x})}{\partial \mathbf{n}} - \int_{S'} \frac{\partial p(\mathbf{x}')}{\partial \mathbf{n}'} \left(G_k(\mathbf{x},\mathbf{x}') + \alpha \frac{\partial G_k(\mathbf{x},\mathbf{x}')}{\partial \mathbf{n}} \right) dS' + f_{inc}. \tag{30}$$

By performing regularization using the Green's function for the Laplace equation, G_0, Eq. (24) is transformed into Eq. (30). While both $\partial^2 G_0 / \partial \mathbf{n} \partial \mathbf{n}'$ and $\partial^2 G_k / \partial \mathbf{n} \partial \mathbf{n}'$ have a singularity of $\mathscr{O}(r^{-3})$, their difference in Eq. (30) has a singularity of $\mathscr{O}(r^{-2})$. Furthermore, the last term inside the braces, which contains only $\partial^2 G_0 / \partial \mathbf{n} \partial \mathbf{n}'$ vanishes at the collocation point $\mathbf{x} = \mathbf{x}'$. Therefore, the regularization has reduced the degree of the singularity in Eq. (30) by one to $\mathscr{O}(r^{-2})$.

Using piecewise constant basis functions on flat elements, Eq. (30) can be discretized as

$$\frac{1}{2}p_i - \sum_{j=0}^{N} p_j \int_{S'_j} \frac{\partial G_k(\mathbf{x}_i,\mathbf{x}')}{\partial \mathbf{n}'} dS'_j - \alpha \Bigg\{ \sum_{j=0}^{N} p_j \int_{S'_j} \left[\frac{\partial^2 G_k(\mathbf{x}_i,\mathbf{x}')}{\partial \mathbf{n}\partial \mathbf{n}'} - \frac{\partial^2 G_0(\mathbf{x}_i,\mathbf{x}')}{\partial \mathbf{n}\partial \mathbf{n}'} \right] dS'_j$$

$$+ \sum_{j=0}^{N} \left[p_j - p_i \right] \int_{S'_j} \frac{\partial^2 G_0(\mathbf{x}_i,\mathbf{x}')}{\partial \mathbf{n}\partial \mathbf{n}'} dS'_j \Bigg\} \tag{31}$$

$$= -\frac{\alpha}{2} q_i - \sum_{j=0}^{N} q_j \int_{S'_j} \left(G_k(\mathbf{x}_i,\mathbf{x}') + \alpha \frac{\partial G_k(\mathbf{x}_i,\mathbf{x}')}{\partial \mathbf{n}} \right) dS'_j + f_{inc}(\mathbf{x}_i),$$

where $p_i = p(\mathbf{x}_i)$ and $q_i = \partial p(\mathbf{x})/\partial \mathbf{n}|_{\mathbf{x}=\mathbf{x}_i}$. This equation can be written in matrix-vector form as follows

$$(\mathbf{A} + \alpha \mathbf{C})\,\mathbf{p} = (\mathbf{B} + \alpha \mathbf{D})\,\mathbf{q} + \mathbf{f}_{inc}, \tag{32}$$

where for the Dirichlet boundary condition $\mathbf{p} = 0$ and for Neumann boundary condition $\mathbf{q} = 0$. The matrix elements in Eq. (32) are given by

$$A_{ij} = \frac{1}{2} - \int_{S'_j} \frac{\partial G_k(\mathbf{x}_i,\mathbf{x}')}{\partial \mathbf{n}'} dS'_j,$$

$$C_{ij} = \begin{cases} \displaystyle\int_{S'_j} \frac{\partial^2 G_k(\mathbf{x}_i,\mathbf{x}')}{\partial \mathbf{n}\partial \mathbf{n}'} dS'_j, & i \neq j, \\ \displaystyle -\int_{S'_j} \left[\frac{\partial^2 G_k(\mathbf{x}_i,\mathbf{x}')}{\partial \mathbf{n}\partial \mathbf{n}'} - \frac{\partial^2 G_0(\mathbf{x}_i,\mathbf{x}')}{\partial \mathbf{n}\partial \mathbf{n}'} \right] dS'_j + \sum_{\ell=1,\neq i}^{N} \int_{S'_\ell} \frac{\partial^2 G_0(\mathbf{x}_i,\mathbf{x}')}{\partial \mathbf{n}\partial \mathbf{n}'} dS'_\ell, & i = j, \end{cases} \tag{33}$$

$$B_{ij} = \int_{S'_j} G_k(\mathbf{x}_i,\mathbf{x}') dS'_j, \;\; D_{ij} = \int_{S'_j} \frac{\partial G_k(\mathbf{x}_i,\mathbf{x}')}{\partial \mathbf{n}} dS'_j.$$

As was mentioned earlier the highest singularity after regularization in Eq. (33) is $\mathscr{O}(r^{-2})$. This type of singularity can be handled by a simple quadrature technique, but the use of a special quadrature rule further improves the solution. This is discussed next.

3.3.2 Duffy's quadrature rule

In applying the Duffy's quadrature rule [10], a flat element is divided into triangles with a common vertex, (x_0, y_0, z_0), at the collocation point. This is shown for a triangular element in Fig. (6). This rule is based on the transformation

$$\begin{aligned} x &= (1-\varepsilon)x_0 + (1-\eta)\varepsilon x_j + \eta\varepsilon x_k, \\ y &= (1-\varepsilon)y_0 + (1-\eta)\varepsilon y_j + \eta\varepsilon y_k, \\ z &= (1-\varepsilon)z_0 + (1-\eta)\varepsilon z_j + \eta\varepsilon z_k, \end{aligned} \tag{34}$$

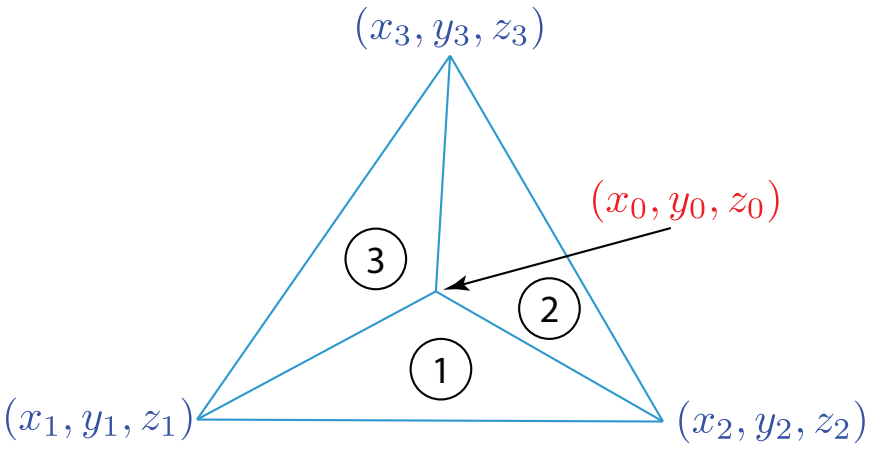

Figure 6: *A triangular element divided into three triangles with a common vertex at the collocation point,* (x_0, y_0, z_0).

where $\varepsilon \leq 1$, $\eta \geq 0$, $j = 1,2,3$ and $k = 2,3,1$ for triangles 1, 2 and 3, respectively. This transformation maps each triangle to a one-square in the positive quadrant of the ε-η plane. Note that the collocation point is reached, i.e., $(x,y,z) = (x_0, y_0, z_0)$, only when $\varepsilon = 0$. Thus kernels that have a singularity at the collocation point are non-singular with respect to η. Additionally, the Jacobian determinant of this transformation is proportional to ε, which further reduces the strength of the singularity.

3.3.3 Application

To demonstrate how non-uniqueness appears in the solution of Eq. (15) when neither CHIEF nor the Burton-Miller methods are used, we computed the far-field backscattered amplitude for a 0.5 m rigid sphere as a function of frequency. In this case, the boundary condition is $\partial p/\partial n|_a = 0$, where a is the radius of the sphere. But if the wavenumber, k, corresponds to the eigenvalues of Eq. (18), which are the eigenvalues of the interior Dirichlet problem, $\partial p/\partial n|_a \neq 0$ and the solution becomes non-unique. The solution is shown in Fig. (7a), where spikes appear at those frequencies where the solution becomes non-unique. The eigenvalues of the interior Dirichlet problem correspond to the zeros of $j_n(k_m a) = 0$, where j_n is the spherical Bessel function of order n. For each n there are m roots and as can be seen in Fig. (7a), the spikes almost exactly occur at the zeros of the spherical Bessel function.

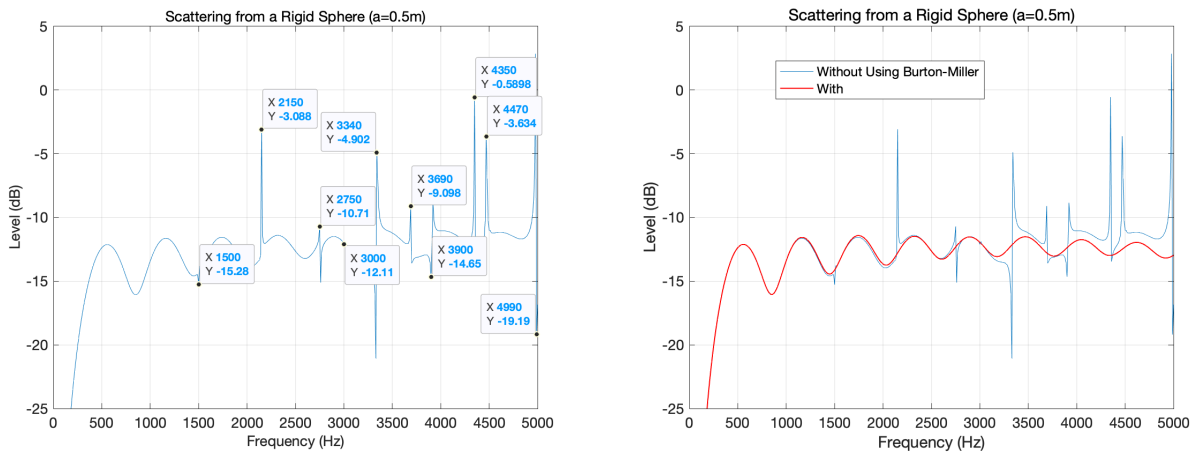

(a) (b)

Figure 7: *Figure (7a) shows the backscattered amplitude as a function of frequency for a rigid sphere computed without the use of CHIEF or Burton-Miller method, necessary to guarantee a unique solution. The solution becomes non-unique at the frequencies that correspond to the eigenvalues of the interior Dirichlet problem, $j_n(k_m a) = 0$. The first 11 zeros of $j_n(k_m a)$ occur at 1500, 2145, 2752, 3000, 3336, 3688, 3906, 4342, 4467, 4500, 5019 Hz, which almost exactly coincide with the frequencies where spikes are seen. Figure (7b) compares the boundary element solutions for two cases, where the Burton-Miller is not used in aquamarine and when it is used in red.*

The use of Burton-Miller (or CHIEF) results in a unique solution and the spikes seen in Fig. (7a) can be eliminated. A comparison between the result in Fig. (7a) and one in which the Burton-Miller has been used is shown in Fig. (7b). Note that non-uniqueness not only exhibits itself in the form of spikes, but it also affects the accuracy of the solution at higher frequencies where spikes proliferate. For this reason, results produced by boundary element methods without the means to deal with non-uniqueness are of little value.

In Fig. (8a) we compare the boundary element solution using the Burton-Miller method in which the Duffy's quadrature rule is used with the exact partial wave solution for backscattering amplitude level as a function *ka* from a 0.5-m rigid sphere. There is excellent agreement between the two solutions. To study the role of Duffy's quadrature rule, in Fig. (8b) we repeat the computation of Fig. (8a) without using the Duffy's method and note that the solution is not as accurate, particularly at higher ka. Since in the Duffy's method each triangular element is divided into three triangular elements, one would think that by tripling the number of elements one should be able to recover the accuracy of the Duffy's method without using it. The green curve in Fig. (8a) shows the results when the number of boundary elements is almost tripled and we see that even though the solution is more accurate than in the case when one third as many elements are used, it is not as accurate as when the Duffy's method is used with a third fewer elements. From this it can be concluded that it is the reduction of the degree of the singularity rather than the number of elements that is responsible for the accuracy of the Duffy's method.

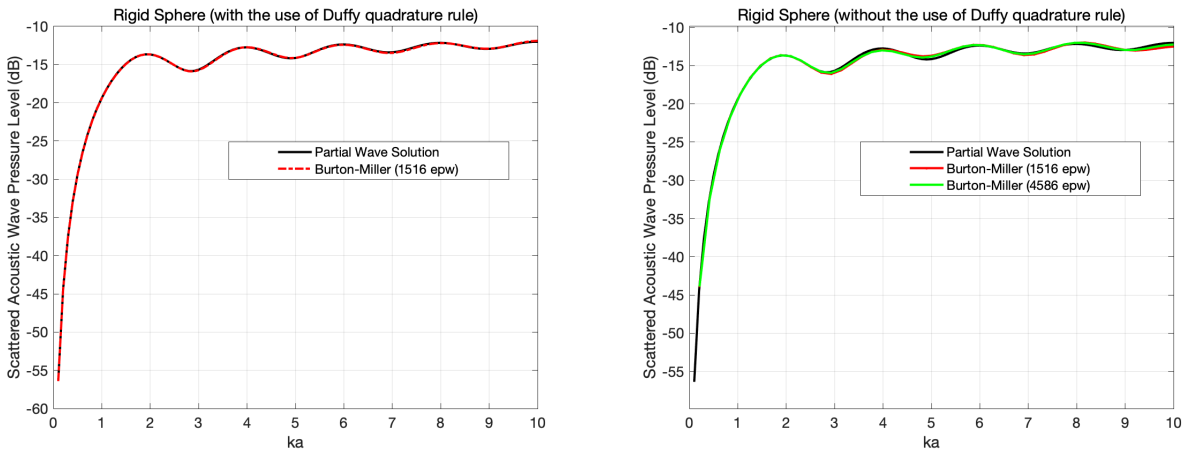

(a) (b)

Figure 8: *Figure (8a) compares the backscattered amplitude level as a function of ka for a rigid sphere–using the Burton-Miller method and the Duffy's quadrature rule– with the exact partial wave solution. In Fig. (8b) the same computation is repeated without the use of Duffy's quadrature rule for the same number of boundary elements as in Fig. (8a) in red and almost triple the number of boundary elements in green.*

4 New model applications

4.1 Computing bi-static scattering amplitudes

One of the objectives of this project has been to compute bi-static scattering amplitudes to support the Target In the Environment Response (TIER) model for complex, non-axially symmetric targets. The TIER model utilizes a fast ray model for propagation of sound to and from a target. The rays are associated with image sources and receivers which account for the interactions with the water-sediment interface. The target scattering piece is reduced to a convolution between the incident acoustic field at the target location and the free-field scattering amplitude from the target. For this purpose, the TIER model needs the far-field bi-static scattering amplitudes on a very dense grid of azimuthal and polar angles. This computation is done in free space, but the information that is provided to TIER enables it to approximately account for the presence of the interface. An example of this type of computation is shown in Fig. (9) where bi-static scattering from a 1:2-foot solid aluminum cylinder is computed on the surface of 10-meter sphere for two incident fields, $\phi_{inc} = 0$ and 60°. The scattering geometry is shown in the bottom right, where the target is centered at the origin with its axis along the y-axis. For each incident angle, over 8000 bi-static scattering amplitudes were computed per octant per frequency. The results shown in Fig. (9) are for a frequency of 30 kHz. The top row in Fig. (9) shows three views of the surface of the sphere in the x-y, x-z and y-z planes for $\phi_{inc} = 0^\circ$, and the bottom row shows the same for $\phi_{inc} = 60^\circ$. Note that for the case of $\phi_{inc} = 0^\circ$, the scattered field is symmetric with respect to both the x-y and the x-z planes, i.e. in the $\pm z$ and $\pm y$ directions, as can be seen in the right and left panels in the top row, respectively. For the case of $\phi_{inc} = 60^\circ$, the field is only symmetric with respect to the x-y plane, as can be seen in the bottom right panel in the bottom row.

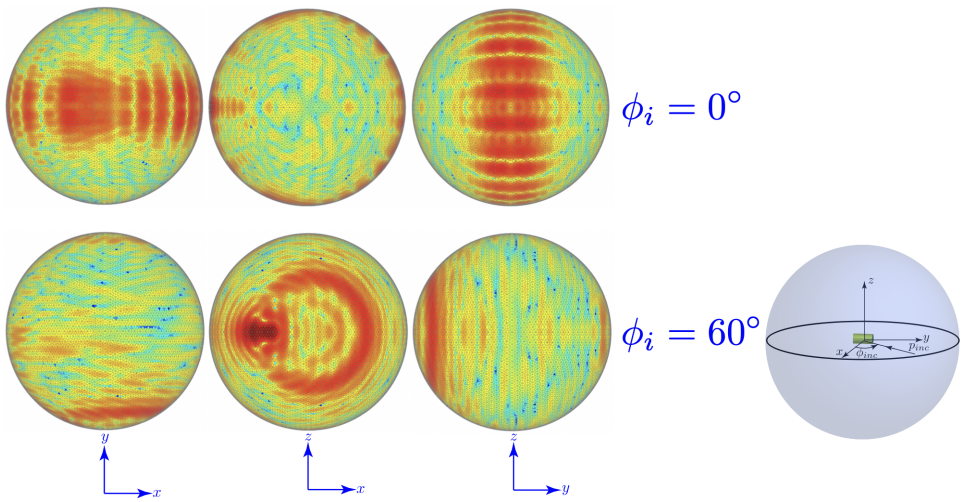

Figure 9: *The bi-static scattering amplitudes from a 1:2-foot solid aluminum cylinder computed on the surface of a 10-meter sphere for two incident fields of* $0°$ *and* $60°$ *at a frequency of 30 kHz. The scattering geometry is shown in the bottom right figure.*

4.2 Scattering in complex environments

The CFBE can compute scattering in any environment provided that the Green's function describing the environment is given in Eq. (A-2). For each of the environment shown in the examples in this section, the appropriate Green's function is used, which is obtained from the exact spectral solution of the wave equation.

Figure (10) shows a model/data comparison of the acoustic color for an aluminum replica of a UXO. The two panels on the left are for the proud case and two the on the right are for the buried case. The geometry of the problem is shown in Fig. (1). In these examples, the bottom is modeled as a half-space with density of 2000 kg m^{-3}, and sound speed of 1694 m s^{-1}. The model/data comparison shows good agreement, as the computed results contain all of the important features seen in the measurement.

Figure (11) shows the acoustic color for an obliquely buried UXO on the left and a UXO buried in a mud layer on the right. The geometry for each case is shown in the top two panels. The example on the left shows that the model can compute scattering from targets in any burial state. In the example on the right the mud layer is sandwiched between the water and sand half spaces (sand is modeled as a heavy fluid, with density of 2000 kg m^{-3}, and sound speed of 1694 m s^{-1}). This demonstrates that the model can also handle more complicated environments. The mud layer in this simulation is approximately 13 cm thick with a density of 1260 kg m^{-3} and sound speed of 1504 m s^{-1}. This is the typical environment in St. Andrew's Bay, where the BAYEX14 was conducted and the mud parameters were those taken from measurements near the experiment site. The middle panel in Fig. (11) shows the acoustic field in the vicinity of the partially buried UXO at a frequency of 20 kHz.

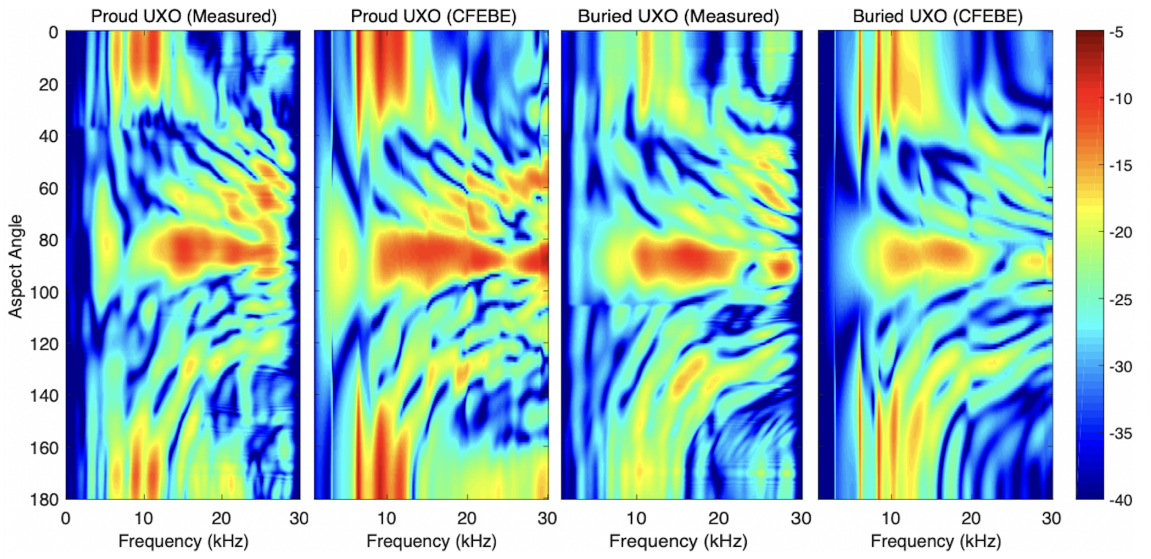

Figure 10: *Comparison of the acoustic color computed by the CFEBE model with measurement for an aluminum replica of a UXO.*

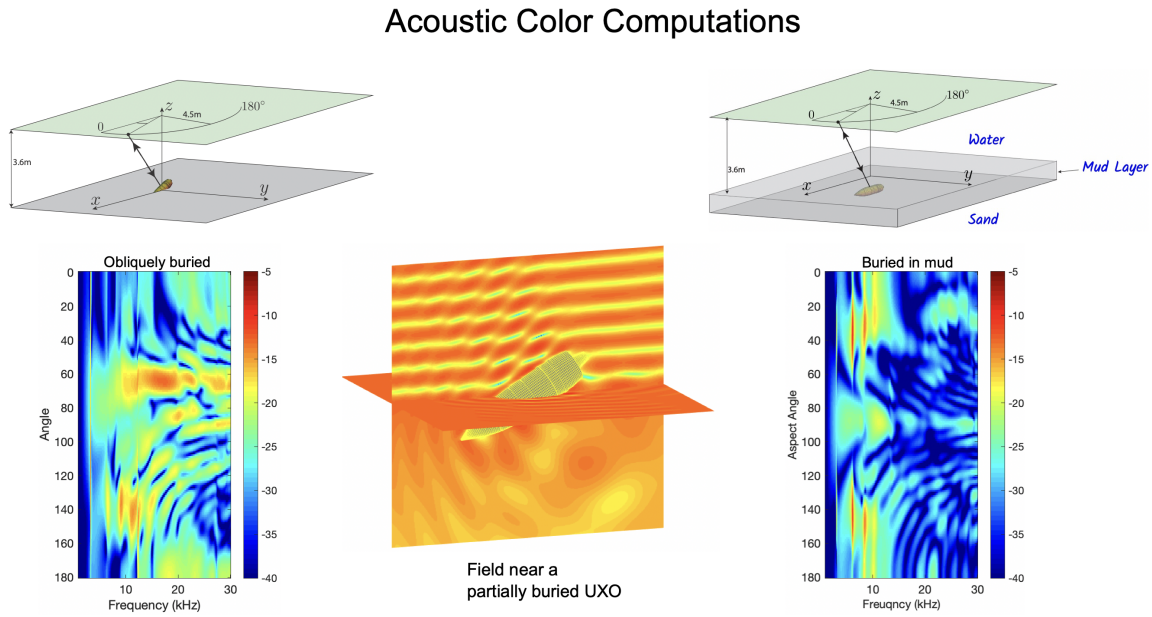

Figure 11: *The acoustic color computed by CFEBE method for a partially buried UXO on the left and one buried in a mud layer on the right. The middle panel shows the acoustic field in the vicinity of the partially buried UXO at a frequency of 20 kHz.*

4.3 Scattering from multiple targets

In the framework of the boundary element method, scattering from a target can be computed using

$$\mathcal{M}\mathbf{p} = \mathbf{p}_{inc}, \tag{35}$$

where the above equation is just Eq. (A-12). This equation can be solved to obtain the surface pressure, and the normal velocity is computed using Eq. (A-14). With the knowledge of these two field quantities, the scattered field can be computed at the receiver.

The matrix $\mathcal{M}$ is called the interaction matrix, which accounts for the interaction between every surface element with every other surface element. If there are n surface elements, $\mathcal{M}$ is a $(n \times n)$ matrix. For instance if the surface of the target is made up of five elements, as shown below, Eq. (35) looks like,

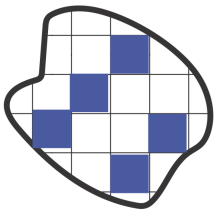

$$\begin{bmatrix} \mathcal{M}_{11} & \mathcal{M}_{12} & \mathcal{M}_{13} & \mathcal{M}_{14} & \mathcal{M}_{15} \\ \mathcal{M}_{21} & \mathcal{M}_{22} & \mathcal{M}_{23} & \mathcal{M}_{24} & \mathcal{M}_{25} \\ \mathcal{M}_{31} & \mathcal{M}_{32} & \mathcal{M}_{33} & \mathcal{M}_{34} & \mathcal{M}_{35} \\ \mathcal{M}_{41} & \mathcal{M}_{42} & \mathcal{M}_{43} & \mathcal{M}_{44} & \mathcal{M}_{45} \\ \mathcal{M}_{51} & \mathcal{M}_{52} & \mathcal{M}_{53} & \mathcal{M}_{54} & \mathcal{M}_{55} \end{bmatrix} \begin{bmatrix} p_1 \\ p_2 \\ p_3 \\ p_4 \\ p_5 \end{bmatrix} = \begin{bmatrix} p_{inc_1} \\ p_{inc_2} \\ p_{inc_3} \\ p_{inc_4} \\ p_{inc_5} \end{bmatrix}, \tag{36}$$

where $\mathcal{M}_{ij}$ represents the interaction between surface elements i and j, $\mathbf{p}_i$ is the surface pressure and $\mathbf{p}_{inc_i}$ is the incident pressure field on element i. In the case of two targets the elements interact with each other and with the elements of the other target as shown below,

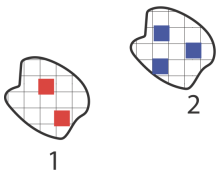

$$\begin{bmatrix} \mathcal{M}_{11} & \mathcal{M}_{12} & \mathcal{M}_{13} & \mathcal{M}_{14} & \mathcal{M}_{15} \\ \mathcal{M}_{21} & \mathcal{M}_{22} & \mathcal{M}_{23} & \mathcal{M}_{24} & \mathcal{M}_{25} \\ \mathcal{M}_{31} & \mathcal{M}_{32} & \mathcal{M}_{33} & \mathcal{M}_{34} & \mathcal{M}_{35} \\ \mathcal{M}_{41} & \mathcal{M}_{42} & \mathcal{M}_{43} & \mathcal{M}_{44} & \mathcal{M}_{45} \\ \mathcal{M}_{51} & \mathcal{M}_{52} & \mathcal{M}_{53} & \mathcal{M}_{54} & \mathcal{M}_{55} \end{bmatrix} \begin{bmatrix} p_1 \\ p_2 \\ p_3 \\ p_4 \\ p_5 \end{bmatrix} = \begin{bmatrix} p_{inc_1} \\ p_{inc_2} \\ p_{inc_3} \\ p_{inc_4} \\ p_{inc_5} \end{bmatrix}, \tag{37}$$

where the matrix is now color-coded to show the interaction between the two targets. The colors red and blue indicate self interaction for target 1 and 2, respectively, and the color green represents interaction between the two targets, where the upper right sub-block in Eq. (37) represents the interaction matrix between target 1 and 2 and the bottom left sub-block represents the interaction between target 2 and 1. Equation (37) can be rewritten as

$$\begin{bmatrix} \mathcal{M}_{11} & \mathcal{M}_{12} \\ \mathcal{M}_{21} & \mathcal{M}_{22} \end{bmatrix} \begin{bmatrix} p_1 \\ p_2 \end{bmatrix} = \begin{bmatrix} p_{inc_1} \\ p_{inc_2} \end{bmatrix}, \tag{38}$$

where the off-diagonal sub-blocks represent the coupling between the two targets and if they are set equal to zero, the targets will become uncoupled, meaning that they each scatter the incident field as if the other were absent. The uncoupled solution, therefore, is the coherent sum of scattering from each target computed separately. The way we solve scattering from multiple targets is the opposite of how the equations are derived here: we first construct the sub-blocks and then assemble the matrix, where the number of sub-blocks for n targets is n^2.

Figure (12) shows the acoustic color for two cylinders as a function of the polar angle. The geometry of the problem is shown in the bottom of each figure. The targets consist of a solid aluminum cylinder (length = 13.75 inch and radius = 2.75 inch diameter) and an open-ended aluminum cylindrical shell (length = 7.6 inch, outer radius = 2 and shell thickness = 1/8 inch). The top row shows the acoustic color for the case when the cylinders are parallel and the bottom row shows the case when the cylindrical shell is tilted by 25°. In the middle column the cylinders are uncoupled by setting the off-diagonal sub-blocks in Eq. (38) to zero. In this case, the scattering accounts for the presence of the two cylinders, but the interaction between them is ignored. The last column shows the difference between the coupled and uncoupled cases, which shows the effects of the coupling as a function of frequency and angle. The coupling is strongest at 90° and 270°, corresponding to broadside angles for both targets. In the bottom left panel where the cylindrical shell is tilted the coupling seems to have weakened when the large cylinder is in the shadow of the cylindrical shell at 90°, but that does not seem to be the case when the opposite occurs at 270°.

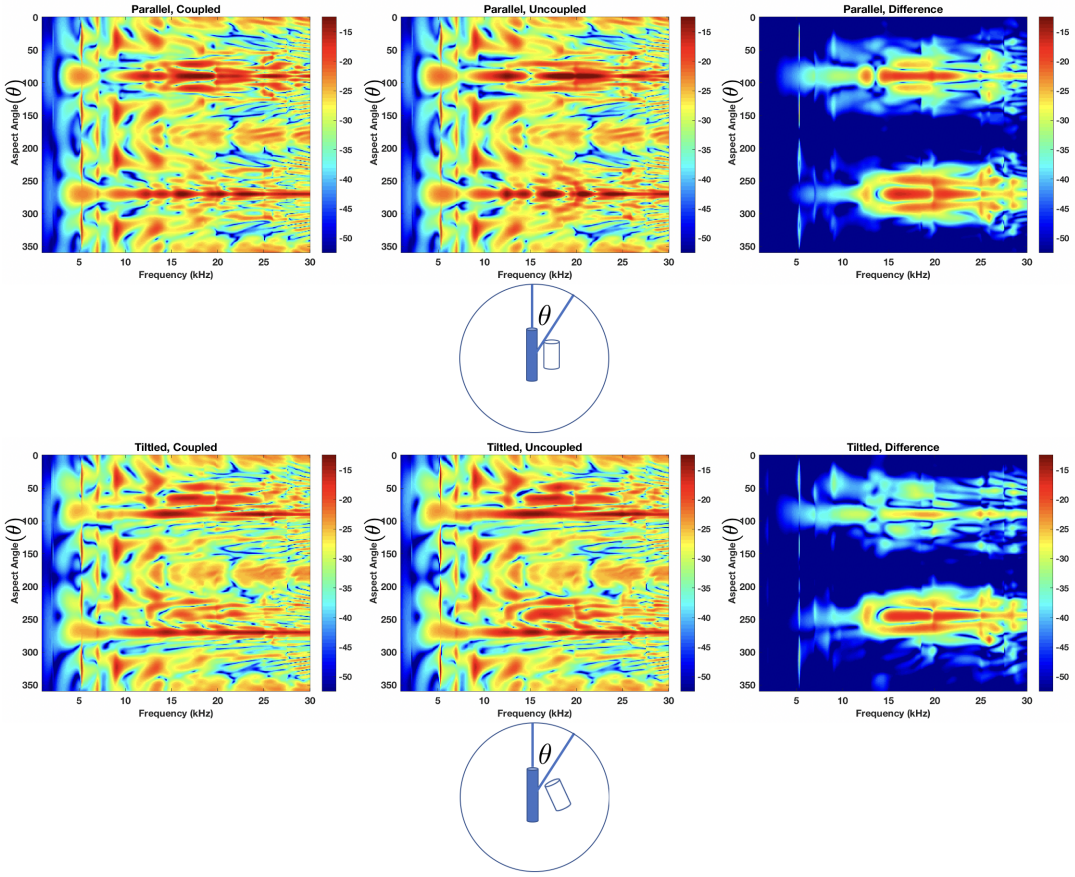

Figure 12: *The acoustic color for two cylinders. In the top row the cylinders are parallel and in the bottom row the cylindrical shell is tilted by 25°. In the middle column the coupling between the two targets is turned off by setting the off-diagonal sub-blocks in Eq. (38) to zero. The right column is the difference between the left and the middle columns. It shows how the coupling varies as a function of frequency and angle.*

The work of Plotnick and Marston [11] in which they measured multiple scattering of an acoustic

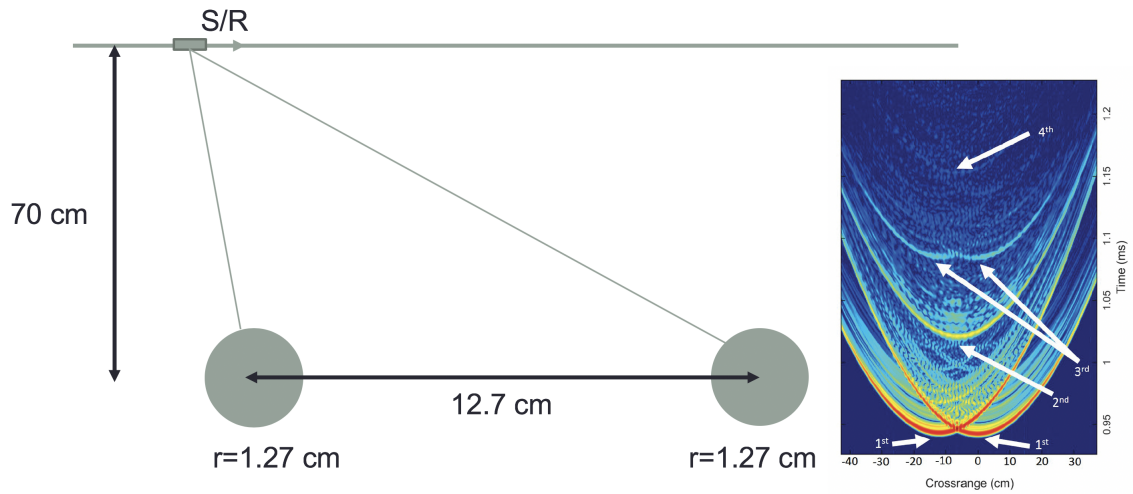

Figure 13: *The cartoon on the left shows the experimental setup. The figure on the right is the recorded data showing multiple arrivals of the scattered signal.*

signal from two identical solid aluminum cylinders, provided a rare opportunity for us to verify that the CFEBE model can correctly account for multiple scattering. The cartoon in the left in Fig. (13) depicts the experimental setup where the track along which the collocated source and receiver (S/R) moved during data collection is illustrated by a straight line. The radii of the cylinders were 1.27 cm and they were separated by 12.7 cm. The S/R were at a height 70 cm above the cylinders and installed on a track, so they could move from left to right. The figure on the right shows the received signal as a function of time, where the horizontal axis is the position of S/R measured from the center of the cylinder on the right, and the vertical axis is time. The crossrange corresponding to about -5 cm is the location where S/R is equidistant to the centers of the two cylinders. The strong returns indicated by 1^{st} are the direct scattered signal from the two cylinders. The rest of the returns, indicated by 2^{nd}, 3^{rd} and 4^{th} are those that are scattered 2, 3 and 4 times, respectively.

If we designate the location of S/R by 0, the right cylinder by 1 and the left cylinder by 2, based on the times of arrival, the returns indicated by 1^{st} in Fig. (13) are due to rays traveling the paths 010 and 020, which are scattered only once by each cylinder. The return indicated by 2^{nd} is composed of two paths one follows the ray path 0120, first scattered by cylinder 1 and then by cylinder 2; and the other follows the ray path 0210, first scattered by cylinder 2 and then by cylinder 1. Similarly, the two ray paths indicated by 3^{rd} are 01210 and 02120, the first experiencing scattering three times, twice by cylinder 1 and once by cylinder 2 and the other twice by cylinder 2 and once by cylinder 1. Higher order returns can be accounted for in a similar way.

Figure(14) shows the acoustic color for this scenario as a function of S/R location along the track. The left panel shows the case when the two cylinders are coupled, which means that not only the scattering from the two cylinders is included, the interaction between them in the form of multiple scattering is also included. In the middle panel, the coupling is turned off by setting the off-diagonal sub-blocks in Eq. (38) to zero. This removes the modulations that is seen in the case

when the cylinders are coupled in the left panel. The right panel shows the difference between the left and the middle panels, which only includes the effect of the coupling between the two cylinders.

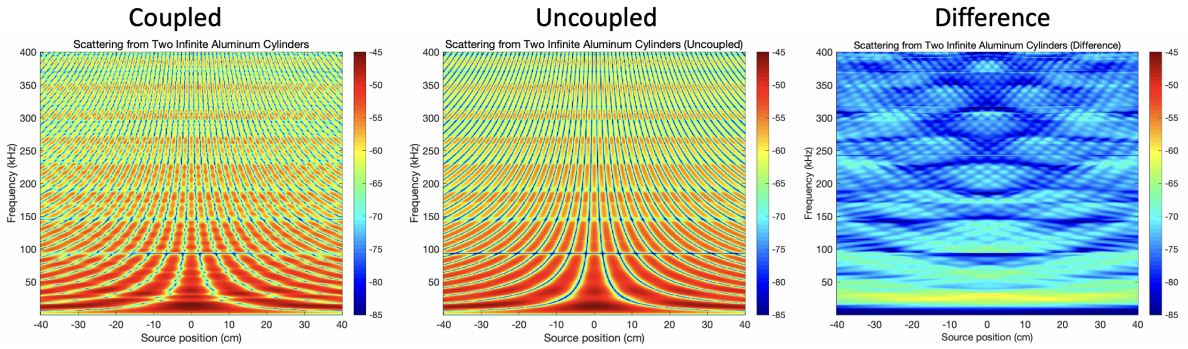

Figure 14: *The acoustic color for the two cylinders shown in Fig. (13). The coupling is turned off in the middle panel by the process described in the text, which results in the removal of modulations seen in the left panel. The right panel shows the difference between the two cases.*

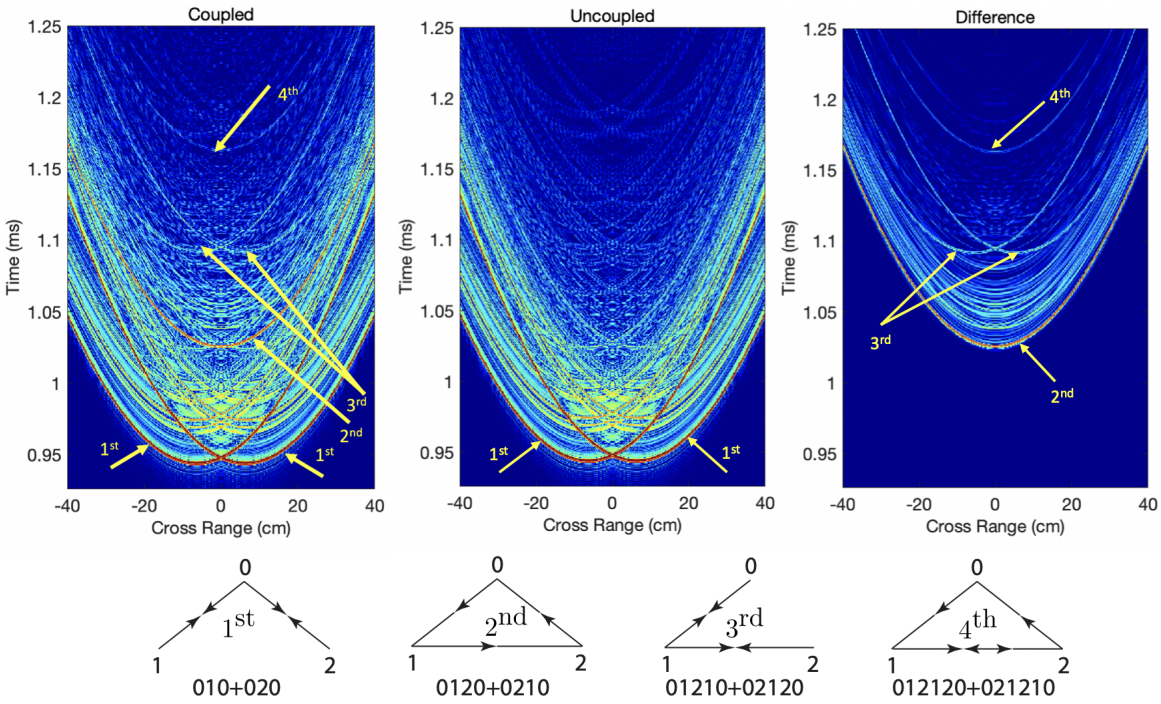

Figure 15: *Modeling results of simulating the experiment shown in Fig. (13). The figure on left shows the full, coupled solution, the one in the middle is the uncoupled solution and the one on the right is the difference between the two solutions, which only contains those returns that experience multiple scattering.*

Figure (15) is obtained by taking the inverse Fourier transform of the results shown in Fig. (14). The figure on the left is the full, coupled solution, which produces the experimental results in

Fig. (13) very closely. This confirms that the model correctly accounts for all physical effects (the complex structure between arrivals in Fig. (13)), and geometrical effects in the form of multiply scattered returns. The middle figure where the coupling is turned off only contains the direct returns from each cylinder and does not contain any of the multiply scattered returns. The figure on the right, shows the coherent difference of the full and the uncoupled solutions and it contains only the multiply scattered returns. This figure, in which most of the elastic responses of the two cylinders present in the left and middle figures is subtracted, also shows two higher-order returns that cannot be seen in the measured data in Fig. (13).

The method described by Eq. (38) was also applied to compute scattering from two 1:2-foot solid aluminum cylinders due to a 10 kHz source located at $(x_s, y_s, z_s) = (4m, 0, 4m)$. In this case the two cylinders are separated by about two meters. The results are shown in Fig. (16) where the figure on the left shows the field in free space and the one on the right shows when the two cylinders are proud in two half-spaces composed of a water half space over a bottom half space with density 2000 kg m^{-3}, and sound speed 1694 m s^{-1}. This solution is an application of Eq. (38) to the case where the two half-space Green's function is used to model the environment.

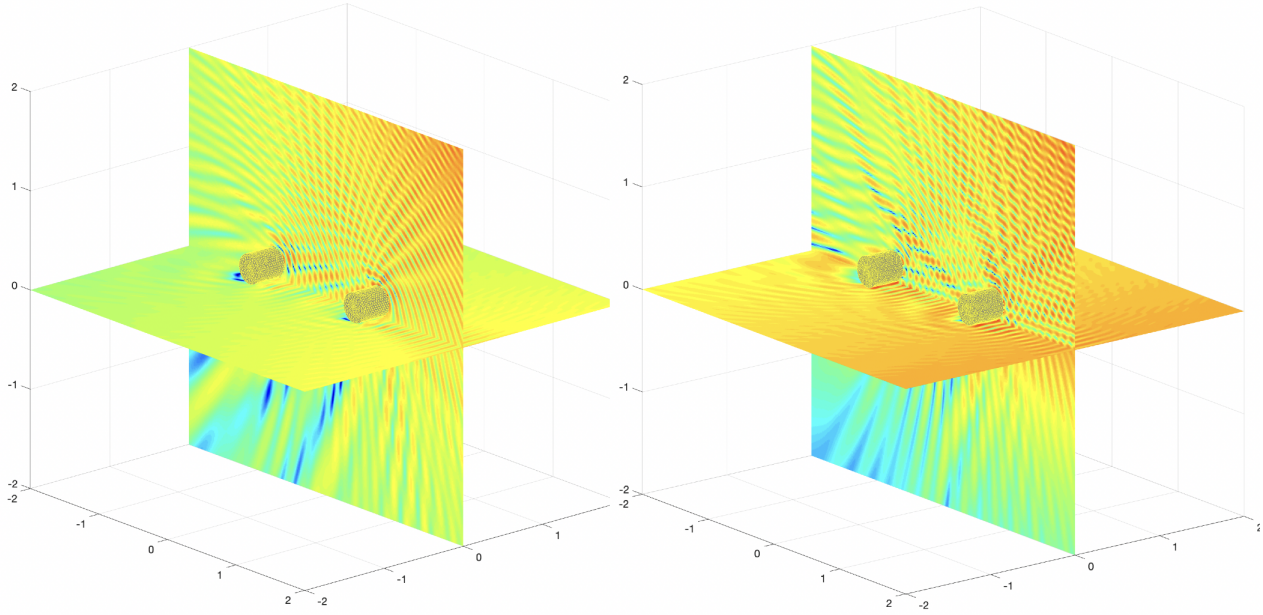

Figure 16: *The 3D field in the vicinity of two 1:2-foot solid aluminum cylinders in free space on the left and proud in two half-spaces on the right.*

Figure (17) shows the acoustic field in a plane perpendicular the axes of the two cylinders in Fig. (16), where the top row is the cylinders in free space and the bottom row is when the cylinders are proud. The left column shows the acoustic field when the coupling is included between the two cylinders, the middle column shows the results when the coupling is turned off and the right column shows the difference between the left and the middle columns, which shows the strength of the coupling. As expected, the coupling is strongest in the vicinity of the line connecting the centers of the two cylinders.

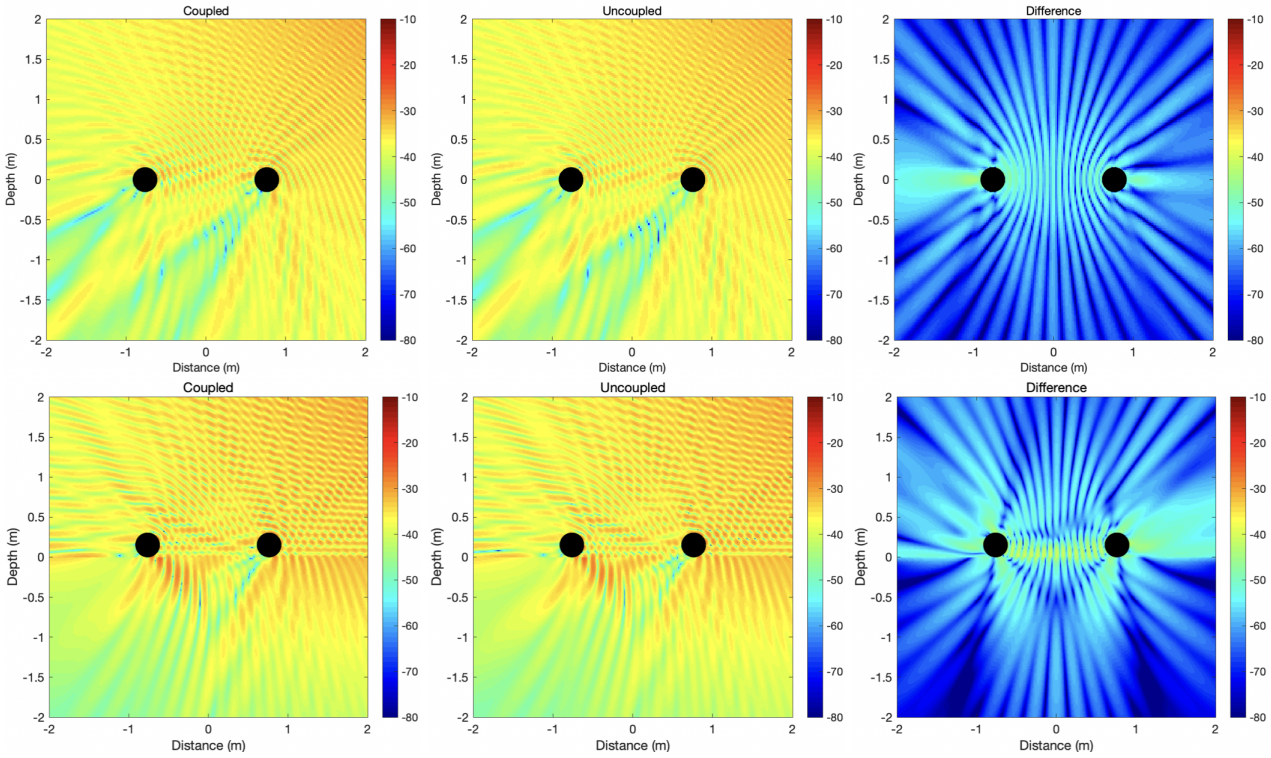

Figure 17: *The acoustic field in the plane perpendicular to the axes of the two cylinders shown in Fig. (16).*

For the case of the proud cylinders, the coupling is strongest between the two cylinders along the interface.

5 Summary and Conclusions

During the first phase of this project (2013-2017), we developed numerical tools to compute scattering from an arbitrary elastic target in an arbitrary ocean environment. These models are based on the fluid-structure interaction method, which uses the finite element method to compute the impedance matrix for the target and the boundary element method to compute the propagation in the environment in which the target is embedded. The two solutions are coupled by imposing the continuity of the pressure and normal particle velocity on the surface of the target. This method produces a system of equations that is self-consistent and rigorously integrates propagation and scattering. This means that it produces a rigorous solution for scattering from an elastic target in any ocean environment that can be characterized by a Green's function. We also developed an axially-symmetric version of the model. This model can be applied to an axially-symmetric target for an arbitrary (not necessarily axially-symmetric) incident field in free space. Since most of the targets of interest are axially-symmetric, this model proves to be very useful. A Final Report for this phase of the project was submitted to SERDP in 2017.

During this phase of the project (2017-2020) we developed a new approach to compute the acoustic color in two half-spaces. This approach is based on using a multipole solution to represent the

spectral Green's functions, which results in significant reduction in computation time. We also laid the groundwork for the implementation of the method of $\mathscr{H}$-Matrices. This method is a hierarchical process of matrix partitioning, which promises to reduce both storage and computation time from $\mathscr{O}(n^2)$ to $\mathscr{O}(n\log n)$, where n is the size of matrices involved. We anticipate that full implementation of this method would be a game changer in modeling scattering from UXOs. We also implemented the Burton-Miller method, which is a perquisite for the implementation of $\mathscr{H}$-Matrices. Furthermore, we developed new applications of the CFEBE model in computing the acoustic color for UXOs in slightly more complex environments and for arbitrary burial. Finally, we constructed a procedure for computing scattering from multiple targets and applied the model to compute scattering from a non-axially symmetric mortar shell.

Appendix A: A new formulation of the fluid-structure problem

The fluid-structure interaction is governed by

$$\begin{bmatrix} \left(-\omega^2\mathbf{M}+\mathbf{K}\right) & \mathbf{L} \\ i\omega\mathbf{B}\mathbf{D}^{-1}\mathbf{L}^{\mathrm{T}} & \mathbf{A} \end{bmatrix} \begin{bmatrix} \mathbf{u} \\ \mathbf{p} \end{bmatrix} = \begin{bmatrix} \mathbf{0} \\ \mathbf{p}_{inc} \end{bmatrix}, \tag{A-1}$$

which relates displacement to force and the surface pressure and normal displacement to the incident pressure field. In the above matrix equation, $\mathbf{M}$ and $\mathbf{D}$ are the structure mass and stiffness matrices and $\mathbf{A}$ and $\mathbf{B}$ are given by

$$A_{mn} = \frac{\delta_{mn}}{2} - \int_{s_n} \frac{\partial G(x_n,x_m)}{\partial n} ds', \qquad B_{mn} = -i\omega\rho \int_{s_n} G(x_n,x_m) ds', \tag{A-2}$$

where G is the environment Green's function. The fluid and structure equations are coupled by the rectangular fluid-structure coupling matrix $\mathbf{L}$, which projects the structure degrees of freedom to the surface degrees of freedom according to

$$L_{i,j} = \int_{s_j} \phi_i(q)\boldsymbol{\Psi}_j(q)\cdot\mathbf{n}_q dS_q, \tag{A-3}$$

where ϕ_i are the fluid and $\boldsymbol{\Psi}_i$ are the structure finite element basis functions and the diagonal matrix $\mathbf{D}$ is given by

$$D_{jj} = \int_{s_j} dS_j. \tag{A-4}$$

The two equations in Eq. (A-1) can be combined to give

$$\left(-\omega^2\mathbf{M} - i\omega\boldsymbol{\mathcal{Z}}_{rad} + \mathbf{K}\right)\mathbf{u} = \mathscr{F}, \tag{A-5}$$

where the structure impedance matrix, $\boldsymbol{\mathcal{Z}}_{rad} = \mathbf{L}\mathbf{A}^{-1}\mathbf{B}\mathbf{D}^{-1}\mathbf{L}^{\mathrm{T}}$, and the force is $\boldsymbol{\mathcal{F}} = -\mathbf{L}\mathbf{A}^{-1}\mathbf{p}_{inc}$. The displacement vector can be written as $\mathbf{u} = [\boldsymbol{\Phi}_s]\{\mathbf{u}_m\}$, where $[\boldsymbol{\Phi}_s]$ is a matrix whose columns

contain the eigenvectors of the structure and $\mathbf{u}_m$ is the modal displacement vector. Substituting for $\mathbf{u}$ in Eq. (A-5) and multiplying the resulting equation from the left by $[\mathbf{\Phi}_s]^{\mathrm{T}}$ gives

$$\left(-\omega^2[\mathbf{\Phi}_s]^{\mathrm{T}}\mathbf{M}[\mathbf{\Phi}_s] - i\omega[\mathbf{\Phi}_s]^{\mathrm{T}}\boldsymbol{\mathcal{Z}}_{rad}[\mathbf{\Phi}_s] + [\mathbf{\Phi}_s]^{\mathrm{T}}\mathbf{K}[\mathbf{\Phi}_s]\right)\{\mathbf{u}_m\} = [\mathbf{\Phi}_s]^{\mathrm{T}}\boldsymbol{\mathcal{F}}. \tag{A-6}$$

For a mass-normalized set of eigenvectors we have, $[\mathbf{\Phi}_s]^{\mathrm{T}}\mathbf{M}[\mathbf{\Phi}_s] = [\mathbf{I}]$, $[\mathbf{\Phi}_s]^{\mathrm{T}}\boldsymbol{\mathcal{Z}}_{rad}[\mathbf{\Phi}_s] = [\mathscr{Z}_{rad_m}]$ and $[\mathbf{\Phi}_s]^{\mathrm{T}}\mathbf{K}[\mathbf{\Phi}_s] = [\Omega_s^2\mathbf{I}]$. This leads to

$$\left(-\omega^2[\mathbf{I}] - i\omega[\mathscr{Z}_{rad_m}] + [\Omega_s^2\mathbf{I}]\right)\{\mathbf{u}_m\} = \{\mathscr{F}_m\}, \tag{A-7}$$

where

$$\{\mathscr{F}_m\} = [\mathbf{\Phi}_s]^{\mathrm{T}}\boldsymbol{\mathcal{F}} = -[\mathbf{\Phi}_s]^{\mathrm{T}}\mathbf{L}\mathbf{A}^{-1}\mathbf{p}_{inc}. \tag{A-8}$$

Combining the above two equations gives

$$\left(-\omega^2[\mathbf{I}] - i\omega[\mathscr{Z}_{rad_m}] + [\Omega_s^2\mathbf{I}]\right)\{\mathbf{u}_m\} = -[\mathbf{\Phi}_s]^{\mathrm{T}}\mathbf{L}\mathbf{A}^{-1}\mathbf{p}_{inc}. \tag{A-9}$$

From the bottom equation in Eq. (A-1) we get the surface pressure

$$\mathbf{p} = \mathbf{A}^{-1}\left(\mathbf{p}_{inc} - i\omega\mathbf{B}\boldsymbol{\Sigma}\right), \tag{A-10}$$

and the normal surface velocity

$$\mathbf{v} = -i\omega\boldsymbol{\Sigma}, \tag{A-11}$$

where $\boldsymbol{\Sigma} \equiv \mathbf{D}^{-1}\mathbf{L}^{\mathrm{T}}\mathbf{u} = \mathbf{D}^{-1}\mathbf{L}^{\mathrm{T}}[\mathbf{\Phi}_s]\{\mathbf{u}_m\}$ and $\{\mathbf{u}_m\}$ is computed using Eq. (A-9). If instead of eliminating $\mathbf{p}$, $\mathbf{u}$ is eliminated in Eq. (A-1), we get the more familiar representation of the boundary element equations with the surface pressure given by

$$\mathbf{p} = \boldsymbol{\mathcal{M}}^{-1}\mathbf{p}_{inc}, \tag{A-12}$$

where

$$\boldsymbol{\mathcal{M}} = \left(\mathbf{A} - i\omega\mathbf{B}\mathbf{L}\left(-\omega^2\mathbf{M} + \mathbf{K}\right)^{-1}\mathbf{L}^{\mathrm{T}}\right), \tag{A-13}$$

is called the interaction matrix. The normal surface velocity given by

$$\mathbf{v} = i\omega\mathbf{L}\left(-\omega^2\mathbf{M} + \mathbf{K}\right)^{-1}\mathbf{L}^{\mathrm{T}}\mathbf{p}. \tag{A-14}$$

With the knowledge of surface pressure and normal velocity, the scattered field can be computed at the receiver locations, x_r, using

$$\mathbf{p}_{scat} = \mathbf{a}^{\mathrm{T}}\mathbf{p} + \mathbf{b}^{\mathrm{T}}\mathbf{v}, \quad \text{where} \quad a_n(x_r) = \int_{s_n} \frac{\partial G(x_r, x')}{\partial n} ds', \quad b_n(x_r) = i\omega\rho \int_{s_n} G(x_r, x') ds'. \tag{A-15}$$

Furthermore, since the continuity of normal displacement requires that the normal velocity in the fluid should be related to the normal displacement in the structure as

$$\mathbf{v} = -i\omega\mathbf{D}^{-1}\mathbf{L}^{\mathrm{T}}\mathbf{u}, \tag{A-16}$$

the bottom equation in Eq. (A-1) can be written as

$$\mathbf{A}\mathbf{p} - \mathbf{B}\mathbf{v} = \mathbf{p}_{inc}. \tag{A-17}$$

References

[1] D. T. Wilton, "Acoustic radiation and scattering from elastic structures," International Journal for Numerical Methods in Engineering, **13**, 123–138 (1978).

[2] A. T. Abawi and P. Krysl, "Coupled finite element/boundary element formulation for scattering from axially-symmetric objects in three dimensions," The Journal of the Acoustical Society of America **142**(6), 3637–3648 (2017).

[3] S. Amini, P. J. Harris, and D. T. Wilton, in *Coupled Boundary and Finite Element Methods for the Solution of the Dynamic Fluid-Structure Interaction Problem* (Springer-Verlag, New York, 1992), Chap. 2 and 4.

[4] M. Bebendorf, *Hierarchical Matrices* (Springer-Verlag, Berlin, Germany, 2008).

[5] S. Börm, L. Grasedyck, and W. Hackbusch, "Hierarchical matrices," Lecture notes **21**, 7 (2003).

[6] H. A. Schenck, "Improved integral formulation for acoustic radiation problems," The Journal of the Acoustical Society of America **44(1)**, 41–58 (1967).

[7] A. J. Burton and G. F. Miller, "The application of integral equation methods to the numerical solutions of some exterior boundary value problems," Proc. R. Soc. London Ser. A **323**, 201–210 (1973).

[8] K. Chen, J. Cheng, and P. J. Harris, "A new study of the burton and miller method for the solution of a 3d helmholtz problem," IMA Journal of Applied Mathematics **74**(2), 163–177 (2008).

[9] W. Meyer, W. Bell, B. Zinn, and M. Stallybrass, "Boundary integral solutions of three dimensional acoustic radiation problems," Journal of Sound and Vibration **59**(2), 245–262 (1978).

[10] M. G. Duffy, "Quadrature over a pyramid or cube of integrands with a singularity at a vertex," SIAM Journal on Numerical Analysis **19**(6), 1260–1262 (1982).

[11] D. Plotnick and P. Marston, "Multiple scattering, layer penetration, and elastic contributions to SAS images using fast reversible processing methods," 11th European Conference on Synthetic Aperture Radar,855–857 (2016).